ARTICLE

https://doi.org/10.1038/s41586-019-1377-y

Modulation of cardiac ryanodine receptor 2 by calmodulin

Deshun Gong[1,5]*, Ximin Chi[1,5], Jinhong Wei[2,5], Gewei Zhou[1], Gaoxingyu Huang[1], Lin Zhang[2], Ruiwu Wang[2], Jianlin Lei[3], S. R. Wayne Chen[2]* & Nieng Yan[1,4]*

The high-conductance intracellular calcium (Ca^{2+}) channel RyR2 is essential for the coupling of excitation and contraction in cardiac muscle. Among various modulators, calmodulin (CaM) regulates RyR2 in a Ca^{2+}-dependent manner. Here we reveal the regulatory mechanism by which porcine RyR2 is modulated by human CaM through the structural determination of RyR2 under eight conditions. Apo-CaM and Ca^{2+}-CaM bind to distinct but overlapping sites in an elongated cleft formed by the handle, helical and central domains. The shift in CaM-binding sites on RyR2 is controlled by Ca^{2+} binding to CaM, rather than to RyR2. Ca^{2+}-CaM induces rotations and intradomain shifts of individual central domains, resulting in pore closure of the PCB95 and Ca^{2+}-activated channel. By contrast, the pore of the ATP, caffeine and Ca^{2+}-activated channel remains open in the presence of Ca^{2+}-CaM, which suggests that Ca^{2+}-CaM is one of the many competing modulators of RyR2 gating.

Cardiac muscle contraction is triggered by Ca^{2+} flux into the cytosol, initially from the extracellular environment, mediated by $Ca_v1.2$, and subsequently from the sarcoplasmic reticulum Ca^{2+} store, mediated by RyR2[1–3]. Ryanodine receptors are the largest known ion channels and consist of a homotetramer with a molecular mass of more than 2 megadaltons. More than 80% of the protein folds into a multi-domain cytoplasmic assembly that senses interactions with a variety of modulators, which range from ions to proteins[4–6]. The precise regulation of RyR2 activity is critical for each heartbeat. Aberrant activity of RyR2 is associated with life-threatening cardiac arrhythmias[7–10].

The 17-kDa protein CaM is an essential calcium sensor that has a central role in most calcium signalling events[11]. CaM consists of roughly symmetrical N- and C-terminal lobes (N- and C-lobes hereafter), joined by a flexible hinge[12,13]. Each lobe can cooperatively bind to two Ca^{2+} ions, with a micromolar-range binding affinity, via two EF-hand (helices E and F-hand) motifs. Upon Ca^{2+} binding, the exposure of several hydrophobic residues in both lobes facilitates CaM binding to the target sequence. CaM interacts directly with ryanodine receptors with a 1:1 stoichiometry of the CaM–RyR protomers[14,15] and binding affinity at nanomolar range[14].

Regulation of ryanodine receptors by CaM, however, is isoform-specific. CaM shows biphasic regulation of RyR1, acting as a weak activator at nanomolar levels of Ca^{2+} (apo-CaM) and an inhibitor at micromolar levels of Ca^{2+} (Ca^{2+}-CaM)[14,16]. By contrast, apo-CaM has no effect[17] or an inhibitory effect on RyR2[14], whereas Ca^{2+}-CaM inhibits RyR2[14]. CaM has also been shown to facilitate the termination of store-overload-induced Ca^{2+} release (SOICR)[18]. Aberrant interactions between CaM and RyR2 are associated with heart failure[19–22], and correction of impaired CaM–RyR2 interactions may serve as a therapy for lethal arrhythmia in pressure-overload-induced heart failure[23].

Structural characterization of RyR–CaM complexes has been limited to low-resolution electron microscopy maps that suggest two overlapping, but distinct, binding sites in RyR1 for apo- and Ca^{2+}-CaM[24–26]. A peptide that corresponds to residues 3614–3643 of RyR1 (residues 3581–3612 in the central domain of RyR2) binds to both apo- and Ca^{2+}-CaM[15,27]. The crystal structure of Ca^{2+}-CaM bound to the peptide revealed hydrophobic anchors in the N and C termini of the peptide that accommodate the C- and N-lobes of Ca^{2+}-CaM, respectively[28].

To elucidate the modulation of RyR2 by CaM, we report eight cryo-electron microscopy (cryo-EM) structures of RyR2 that collectively reveal molecular recognition characteristics for different forms of CaM and provide insights into the regulation of RyR2 channel gating by CaM.

Structures of RyR2 under eight conditions

To achieve a better understanding of RyR2 modulation by CaM (Extended Data Fig. 1a, b), we determined the cryo-EM structures of the porcine RyR2 (Extended Data Fig. 1c) under the following eight conditions.

Condition (1) consisted of RyR2 bound to FKBP12.6 and apo-CaM (hereafter FKBP12.6/apo-CaM) and was used to assess the apo-CaM binding site. Condition (2) consisted of RyR2 bound to FKBP12.6 and a Ca^{2+}-binding-deficient CaM mutant that mimics apo-CaM[24,29] (CaM-M) in the presence of ATP, caffeine and low [Ca^{2+}] (hereafter FKBP12.6/ATP/caffeine/low-[Ca^{2+}]/CaM-M), this structure was used to investigate the mechanism for the binding-location switch of CaM. Condition (3) consisted of RyR2 bound to FKBP12.6 in the presence of ATP, caffeine and low [Ca^{2+}] (FKBP12.6/ATP/caffeine/low-[Ca^{2+}]), the presence of which maximizes the open state. Condition (4) consisted of RyR2 bound to FKBP12.6 and Ca^{2+}-CaM in the presence of ATP, caffeine and low [Ca^{2+}] (hereafter FKBP12.6/ATP/caffeine/low-[Ca^{2+}]/Ca^{2+}-CaM); this condition was used to examine the effect of Ca^{2+}-CaM on the open RyR2 channel in the presence of FKBP12.6, ATP, caffeine and low [Ca^{2+}]. Conditions (5) and (6) corresponded to conditions (3) and (4), respectively, but were treated with CHAPS and DOPC instead of digitonin. Condition (7) consisted of RyR2 in high [Ca^{2+}] in the presence of FKBP12.6, ATP, caffeine and Ca^{2+}-CaM

[1]Beijing Advanced Innovation Center for Structural Biology, Tsinghua-Peking Joint Center for Life Sciences, School of Life Sciences, Tsinghua University, Beijing, China. [2]Libin Cardiovascular Institute of Alberta, Department of Physiology and Pharmacology, University of Calgary, Calgary, Alberta, Canada. [3]Technology Center for Protein Sciences, Ministry of Education Key Laboratory of Protein Sciences, School of Life Sciences, Tsinghua University, Beijing, China. [4]Present address: Department of Molecular Biology, Princeton University, Princeton, NJ, USA. [5]These authors contributed equally: Deshun Gong, Ximin Chi, Jinhong Wei. *e-mail: gds13@tsinghua.org.cn; swchen@ucalgary.ca; nyan@princeton.edu

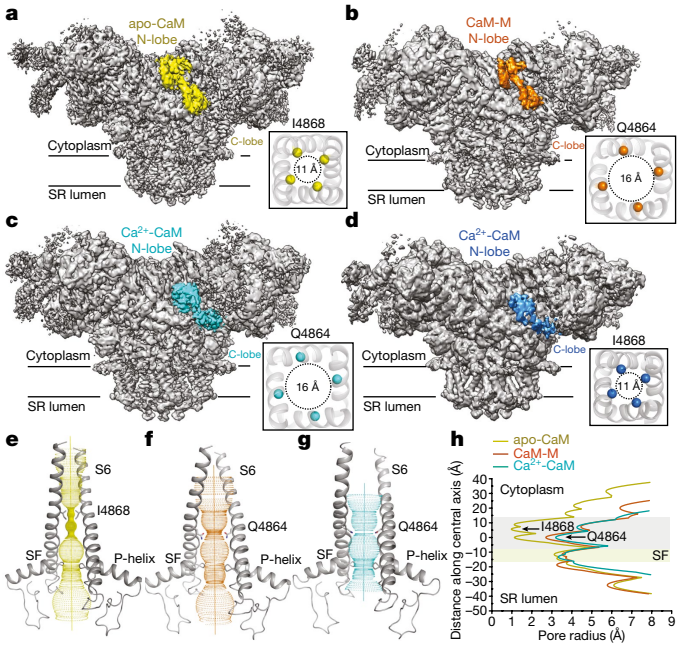

Fig. 1 | Cryo-EM structures of the RyR2–CaM complexes. a–d, Overall electron microscopy maps for four indicated complexes. **a**, RyR2 in the presence of FKBP12.6/apo-CaM (3.6 Å). **b**, RyR2 in the presence of FKBP12.6/ATP/caffeine/low [Ca^{2+}]/CaM-M (4.2 Å). **c**, RyR2 in the presence of FKBP12.6/ATP/caffeine/high [Ca^{2+}]/Ca^{2+}-CaM (3.9 Å). **d**, RyR2 in the presence of PCB95/low-[Ca^{2+}]/Ca^{2+}-CaM (4.4 Å). Insets, cytoplasmic views of the channel gates. The dashed circles indicate the distances between the C_α atoms of the gating residues in the diagonal protomers. See Extended Data Table 1 for details of the structures. SR, sarcoplasmic reticulum. **e**, The pore of RyR2 remains closed in the FKBP12.6/apo-CaM structure. The ion permeation path, calculated by HOLE[41], is illustrated as yellow dots. SF, selectivity filter. **f**, **g**, Open pores of RyR2 in FKBP12.6/ATP/caffeine/low-[Ca^{2+}]/CaM-M (**f**) and FKBP12.6/ATP/caffeine/high-[Ca^{2+}]/Ca^{2+}-CaM (**g**). **h**, The corresponding pore radii of RyR2 for the three structures shown in **e**–**g**. Electron microscopy maps were generated in Chimera and contoured at levels of 0.027, 0.022, 0.02 and 0.015 for **a**–**d**, respectively. All structures were prepared using PyMOL (http://www.pymol.org).

(hereafter FKBP12.6/ATP/caffeine/high-[Ca^{2+}]/Ca^{2+}-CaM); this environment was used to achieve a better resolution for Ca^{2+}-CaM. Condition (8) consisted of RyR2 bound to Ca^{2+}-CaM in the presence of 2,2′,3,5′,6-pentachlorobiphenyl (PCB95) and low [Ca^{2+}] (hereafter PCB95/low-[Ca^{2+}]/Ca^{2+}-CaM); this condition was used to investigate the effect of Ca^{2+}-CaM on PCB95 and the Ca^{2+}-activated RyR2 channel[30]. The eight conditions and corresponding structures are summarized in Supplementary Table 1 and Extended Data Table 1, respectively.

All cryo-EM datasets were processed following the same procedure (Extended Data Fig. 2). The FKBP12.6/apo-CaM RyR2 structure was determined at an overall resolution of 3.6 Å, the highest among all of the available RyR2 structures (Fig. 1a and Extended Data Figs. 1i, 3a, 4a–i). The secondary structural elements of apo-CaM were clearly resolved (Fig. 1a and Extended Data Fig. 3b). The FKBP12.6/ATP/caffeine/low-[Ca^{2+}]/CaM-M RyR2 structure was determined at an overall resolution of 4.2 Å, in which the well-resolved CaM-M is positioned similarly to apo-CaM on RyR2 (Fig. 1b and Extended Data Figs. 1i, 3c, d). The densities for both lobes of Ca^{2+}-CaM are visible in the FKBP12.6/ATP/caffeine/high-[Ca^{2+}]/Ca^{2+}-CaM RyR2 structure (3.9 Å resolution) and PCB95/low-[Ca^{2+}]/Ca^{2+}-CaM RyR2 structure (4.4 Å resolution) in which the N-lobe is better-resolved than the C-lobe. By contrast, only one lobe of Ca^{2+}-CaM—the N lobe as judged from the comparison with the structure of FKBP12.6/ATP/caffeine/high-[Ca^{2+}]/Ca^{2+}-CaM at 3.9 Å—is discernible in the FKBP12.6/ATP/caffeine/low-[Ca^{2+}]/Ca^{2+}-CaM structure with a resolution of 4.2 Å (Fig. 1c, d and Extended Data Figs. 1, 3).

With regard to the gating state of the eight structures reported here, the clearly resolved Ile4868 residues on the S6 helical bundle of FKBP12.6/apo-CaM constitute the constriction site with a radius of approximately 1 Å, which is identical to the previously reported apo-RyR2 in the closed state[30] (Fig. 1e, h). The constriction site appears to shift to Gln4864 with an expanded radius of around 3 Å in conditions (2), (3) and (5)–(7) (Fig. 1f–h and Extended Data Fig. 1d, h), similar to that in the open PCB95/low-[Ca^{2+}] structure[30]. However, the density for the side chain of Gln4864 in FKBP12.6/ATP/caffeine/low-[Ca^{2+}]/Ca^{2+}-CaM is not well-resolved. We, therefore, compared the distances of C_α atoms of the gating residues in the diagonal protomers, which are approximately 16 Å for FKBP12.6/ATP/caffeine/low-[Ca^{2+}]/Ca^{2+}-CaM and 11 Å for FKBP12.6/apo-CaM (Fig. 1a and Extended Data Fig. 1e). The constriction site in PCB95/low-[Ca^{2+}]/Ca^{2+}-CaM is constituted by Ile4868, for which the diagonal distance of the C_α atoms is approximately 11 Å—similar to that in FKBP12.6/apo-CaM (Fig. 1a, d).

As seen in RyR1, the Ca^{2+}-, ATP- and caffeine-binding sites are located at the interfaces between the central and channel domains of RyR2[31] (Extended Data Fig. 4j–m).

Location of apo-CaM in RyR2

Consistent with the low-resolution structure of RyR1, apo-CaM is located in an elongated cleft formed by the handle, helical and central domains of RyR2 in FKBP12.6/apo-CaM[24,25] (Fig. 2a). The N-lobe is stuck in the upper half of the cleft formed by helical domain 1 (HD1), whereas the C-lobe is located at the bottom edge of the cleft surrounded by the handle and central domains of RyR2 (Fig. 2a).

The FKBP12.6/apo-CaM structure reveals five surface patches on RyR2 that interact with apo-CaM. The N-lobe interacts with RyR2 through three interfaces that are mainly located in HD1 (Fig. 2b and Extended Data Fig. 5a). The most prominent interface is formed between the N terminus of helix 4 (N4) in the N-lobe and the C termini of helices 2b and α1 in HD1, and is mainly mediated by extensive hydrophobic residues. Phe66, Pro67 and Leu70 on N4 probably interact with Tyr2203 in helix 2b and Tyr2157 (human Tyr2156) in helix α1. Ile10 in N1 may also interact with Tyr2157 (Extended Data Fig. 5a, g). The human Y2156C variant is linked to catecholaminergic polymorphic ventricular tachycardia[8]. The second interface is mediated by charged residues between the N terminus of N1 in the N-lobe and helix α1 in HD1 and the N terminus of helix α0 in the central domain. The third interface is formed between a region rich in acidic residues in N3 of the N-lobe and Lys2558 in helix 8b of HD1 (Fig. 2b and Extended Data Fig. 5a).

The C-lobe interacts with RyR2 through two interfaces (Fig. 2c). One is consistent with previous reports[15,27]. Residues 3593–3607 in the central domain folds into a newly resolved helix α 'minus 1' (helix α−1) that is enclosed by the hydrophobic cavity of the C-lobe, representing the primary interface. Phe3604 serves as a hydrophobic anchor for the hydrophobic cavity of the C-lobe. A minor interface is formed between helix 12 and the C terminus of helix 11 in the handle domain with the C terminus of C1 and the loop between C2 and C3 in the C-lobe, also through hydrophobic interactions (Fig. 2c and Extended Data Fig. 5b, c, h).

Shift of CaM-binding site in RyR2 after Ca^{2+} loading

CaM markedly slips down along the cleft after Ca^{2+} loading, making extensive interactions with the central domain (Fig. 2d). The N-lobe is anchored by the central domain and the C-lobe drops beyond the cleft, coordinated only by helix α−1 (Fig. 2d). The limited contact may explain the structural flexibility of the C-lobe.

The binding of Ca^{2+}-CaM with intact RyR2 is similar to that of Ca^{2+}-CaM with the RyR1 peptide[28]. The N- and C-lobes of CaM interact with the C- and N termini of helix α−1, respectively (Fig. 2d). Phe3604 and Trp3588 anchor the hydrophobic cavities of the N- and C-lobes, respectively (Extended Data Fig. 5d–f, i). An additional interface is formed between the N terminus of N3 and the C terminus of helix α9 in the central domain to further stabilize the binding of N-lobe. Asp51

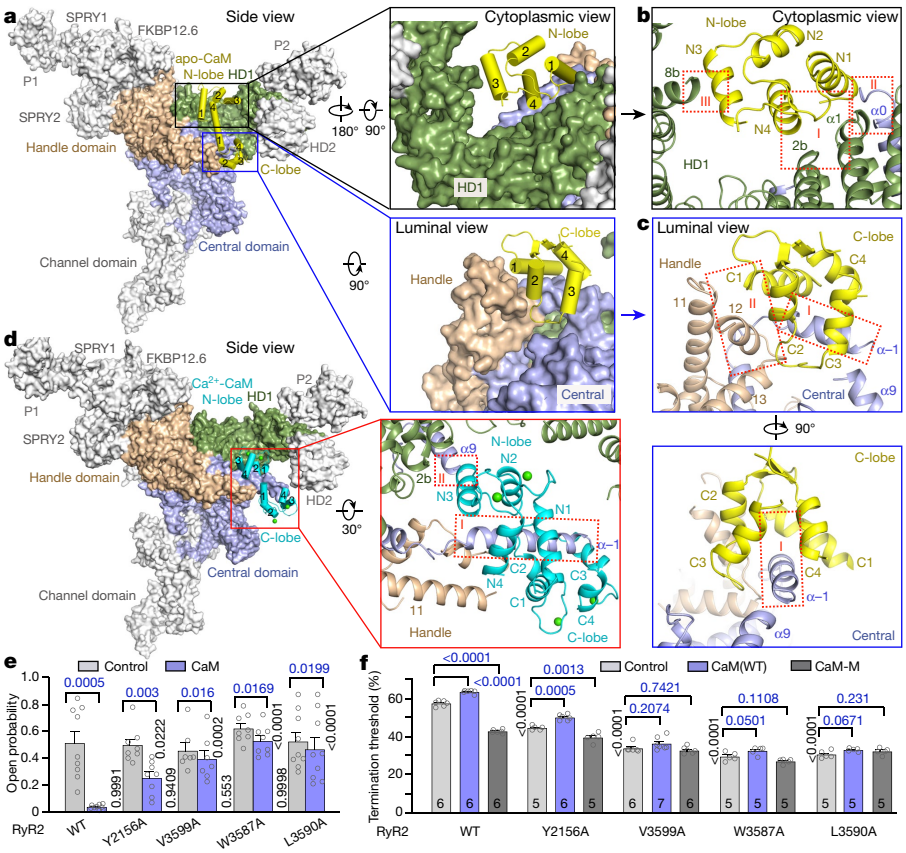

Fig. 2 | Interfaces between CaM and RyR2. a, Apo-CaM is located in a cleft formed by the handle, helical and central domains of RyR2. One RyR2 protomer is shown in domain-coloured surface view. **b**, **c**, Multiple interfaces between RyR2 and apo-CaM. The red, dashed boxes indicate the interfaces. **d**, A previously unresolved helix α−1 on RyR2 serves as the primary docking site for both lobes of Ca^{2+}-CaM. **e**, Functional validation of the observed interfaces between mouse RyR2 and human CaM. Open probabilities of single RyR2 channels before (control) and after addition of CaM(WT) (1 μM). Data are mean ± s.e.m. from RyR2(WT) ($n = 9$), RyR2(Y2156A) ($n = 8$), RyR2(V3599A) ($n = 7$), RyR2(W3587A) ($n = 8$) and RyR2(L3590A) ($n = 9$ single channels) and analysed by paired, two-sided Student's *t*-test (versus its own control) with *P* values shown in blue and by one-way analysis of variance (ANOVA) with a Dunnett's post hoc test (versus RyR2(WT) control and RyR2(WT) with CaM(WT), respectively) with adjusted *P* values shown in black. **f**, The termination threshold of Ca^{2+} release in $Ryr2^{WT}$- and *Ryr2*-mutant-expressing HEK293 cells transfected with no CaM (control), CaM(WT) or CaM-M. Data are mean ± s.e.m. with the number of independent experiments for each condition shown and analysed by one-way ANOVA with a Dunnett's post hoc test with adjusted *P* values shown in blue (versus its own control) and in black (versus RyR2(WT) control).

in N3 probably interacts with Arg2209 in helix 2b of HD1 (Fig. 2d and Extended Data Fig. 5e).

Functional validation of RyR2–CaM interfaces

We assessed the effect of mutations in RyR2 and CaM that are located in the structurally revealed interfaces on CaM regulation of RyR2. Wild-type CaM (CaM(WT)) strongly reduced the open probability of single wild-type mouse RyR2 (RyR2(WT)) channels. The following mutations markedly reduced CaM inhibition of single RyR2 channels: RyR2(Y2156A) (porcine Y2157A) near an interface between the apo-CaM N-lobe and RyR2, RyR2(V3599A) near both the apo-CaM C-lobe–RyR2 and Ca^{2+}-CaM N-lobe–RyR2 interfaces, and RyR2(W3587A) and RyR2(L3590A) near the Ca^{2+}-CaM C-lobe–RyR2 interface (Fig. 2e and Extended Data Fig. 6).

We next examined the effect of these RyR2 mutations on the termination of RyR2-mediated SOICR. As previously shown[18], CaM(WT) increased Ca^{2+} release termination in RyR2(WT)-expressing HEK293 cells, whereas CaM-M reduced Ca^{2+} release termination (that is, a longer calcium release) (Fig. 2f and Extended Data Fig. 7a–c). Consistent with their effect on single RyR2 channels, all four mutations in RyR2 significantly reduced Ca^{2+} release termination in HEK293 cells, probably by impairing the effect of endogenous CaM on RyR2 inhibition (Fig. 2f). These RyR2 mutations also reduced or abolished the effect of exogenously expressed CaM(WT) and CaM-M on Ca^{2+} release termination (Fig. 2f), but had little or no effect on SOICR activation or store capacity (Extended Data Fig. 7d, e).

We also assessed the functional importance of CaM residues near the RyR2–CaM interfaces. Mutations in CaM near the apo-CaM N-lobe–RyR2(K2153/Y2156) interface (CaM(E15A), CaM(F66A) and CaM(L70A)), near the apo-CaM C-lobe–RyR2(V3599) interface (CaM(M110A) and CaM(F142A)), near the Ca^{2+}-CaM N-lobe–RyR2(V3599) interface (CaM(F20A) and CaM(F69A)) and near the Ca^{2+}-CaM C-lobe–RyR2(W3587/L3590) interface (CaM(F93A), CaM(L106A) and CaM(M146A))—as with CaM-M—significantly reduced the effect of CaM on Ca^{2+} release termination compared to CaM(WT) (Extended Data Fig. 7f). All CaM mutations except for CaM(F20A) and CaM(F142A) had little or no effect on SOICR activation or store capacity (Extended Data Fig. 7g, h). Note that some mutations in CaM may induce conformational changes, thus affecting CaM–RyR2 interactions allosterically. Collectively, these functional studies support the importance of the newly identified RyR2–CaM interfaces in CaM regulation of RyR2.

Ca^{2+}-dependent shift in CaM-binding sites on RyR2

The location and conformation of CaM-M and apo-CaM are identical in the structures (Fig. 3a), which suggests that the positional switch for apo-CaM and Ca^{2+}-CaM results from the distinct conformations of CaM after Ca^{2+} loading instead of a direct effect of Ca^{2+} on RyR2. The CaM lobes have previously been reported in three

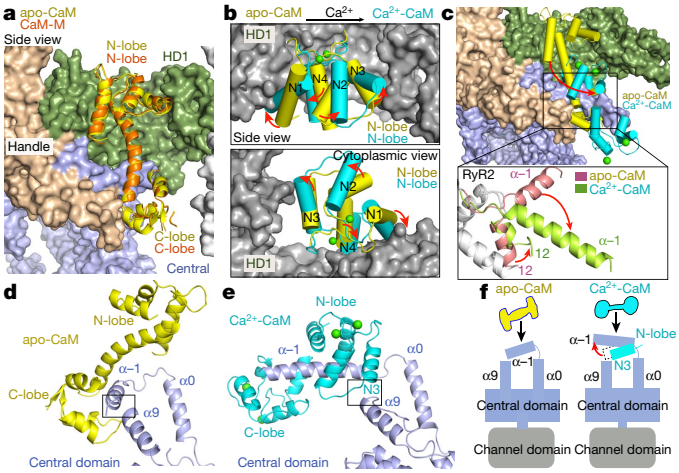

Fig. 3 | Molecular basis for the shift of binding site for CaM after Ca^{2+} loading. a, Ca^{2+} binding to RyR2 is not responsible for the positional shift in apo-CaM and Ca^{2+}-CaM. In the presence of 20 μM Ca^{2+}, the binding site for CaM-M remains the same as for apo-CaM. The two structures are superimposed relative to CaM. **b**, Upon Ca^{2+} loading, the expansion of CaM structure may lead to steric hindrance between the N-lobe and HD1. The N-lobes are superimposed. Red arrows indicate directions of conformational changes from apo-CaM to Ca^{2+}-CaM. **c**, The shift in the CaM-binding site is accompanied by marked conformational changes in helices α−1 and 12 in RyR2. Red arrows indicate the conformational changes in RyR2 from FKBP12.6/apo-CaM to FKBP12.6/ATP/caffeine/high-[Ca^{2+}]/Ca^{2+}-CaM. **d**, In FKBP12.6/apo-CaM, helix α−1 contacts helix α9. **e**, In FKBP12.6/ATP/caffeine/high-[Ca^{2+}]/Ca^{2+}-CaM, helix α−1 of RyR2 is positioned away from helix α9. Helix N3 in the N-lobe contacts helix α9 instead. **f**, Helix α−1 of RyR2 serves as an essential anchor for CaM. Red arrow indicates the direction of conformational change of helix α−1 from FKBP12.6/apo-CaM to FKBP12.6/ATP/caffeine/high-[Ca^{2+}]/Ca^{2+}-CaM.

conformations—open, semi-open and closed—when interacting with other proteins[32–34]. Comparative docking analysis of these conformations into the electron microscopy reconstruction for FKBP12.6/ATP/caffeine/high-[Ca^{2+}]/Ca^{2+}-CaM suggests an open conformation for the N-lobe (Extended Data Fig. 8a, b). An important distinction between the open and semi-open or closed C-lobes is the slightly larger helical angle between C1 and C4, both of which were resolved in the map and conformed to the open state (Extended Data Fig. 8c, d).

These analyses are consistent with the observations in the crystal structure of RyR1 peptide-bound Ca^{2+}-CaM[28]. Upon Ca^{2+} loading, the compact structure of apo-CaM is relaxed to Ca^{2+}-CaM[35], which slips down towards the N-terminal part of helix α−1, consistent with previous studies[36].

Helix α−1 and helix 12 are two helices that were only resolved in the structures with CaM, probably owing to stabilization of these segments through CaM binding. Pronounced shifts in these two helices are observed between the structures bound to apo-CaM and Ca^{2+}-CaM. In the presence of Ca^{2+}-CaM, helix α−1 swings by around 90° and the N-terminal half of helix 12 also bends by nearly 90° (Fig. 3c). Accordingly, helix α−1, which contacts helix α9 of the central domain in FKBP12.6/apo-CaM, is positioned away from helix α9 in FKBP12.6/ATP/caffeine/high-[Ca^{2+}]/Ca^{2+}-CaM. Now helix α9 is in contact with helix 3 in the N-lobe of Ca^{2+}-CaM (Fig. 3d–f). The CaM-bound RyR2 structures shown here reveal that helix α−1 serves as an essential anchor for CaM (Fig. 3f).

Inhibitory modulation of RyR2 by Ca^{2+}-CaM

Both caffeine and ATP are located at the interfaces between the U-motif and O-ring, locking them into a stable unit that stabilizes the open state (Extended Data Fig. 9a). Caffeine and ATP counteract inhibitory effect of Ca^{2+}-CaM on RyR2, manifested by the lack of intradomain change of individual central domains. The pore remains open (Extended Data Figs. 1e, 9b). Nevertheless, Ca^{2+}-CaM induces an anticlockwise rotation of the central domains in the cytoplasmic view in the same direction as that from the open to the closed state[30,37] (Extended Data Fig. 9c and Supplementary Video 1). The central domains undergo similar shifts in the presence of high concentrations of Ca^{2+} and CaM, but not in the CHAPS plus DOPC condition (Extended Data Fig. 10a, b).

By contrast, RyR2 activated by PCB95 and Ca^{2+} is closed after addition of Ca^{2+}-CaM (Fig. 1d). Detailed structural examination shows an anticlockwise rotation of the central domains and outward motions of the auxiliary motifs of the individual central domain, including helices α0, α1, α4 and the U-motif, with respect to the centre of the concave surface (Extended Data Figs. 9d, 10c). The motion of the U-motif appears to release the pulling force for the dilation of the S6 helix, resulting in closure of the pore (Extended Data Fig. 9e). Taken together, these results indicate that the inhibitory force of Ca^{2+}-CaM is sufficient to overcome the synergistic activation of RyR2 by PCB95 and Ca^{2+}, but not by the collective effect of ATP, caffeine and Ca^{2+} (Fig. 4).

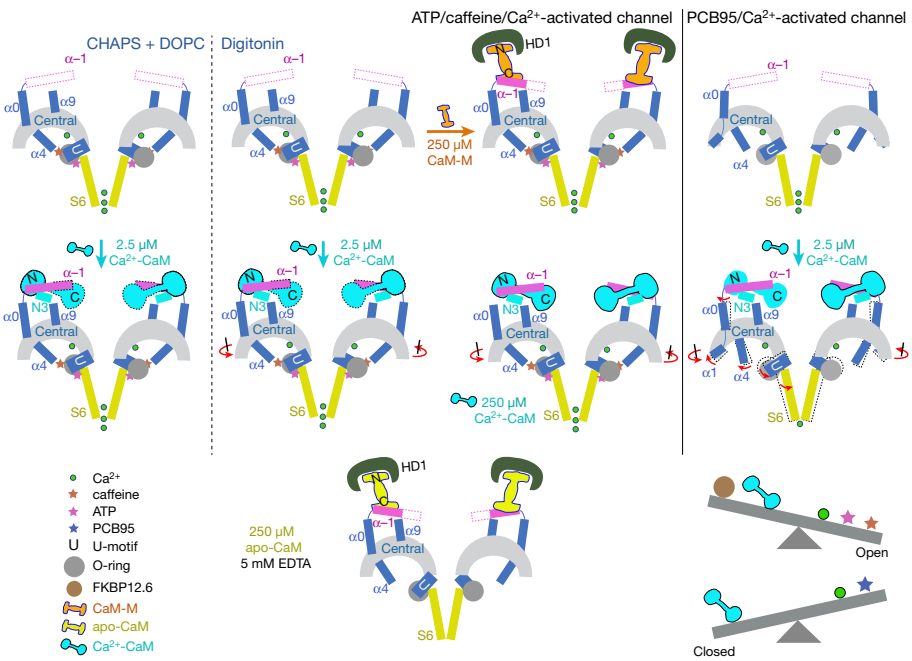

Fig. 4 | Schematic of RyR2 modulation by CaM. The two RyR2 structures on the left were obtained in the presence of CHAPS and DOPC instead of digitonin, which was used for all other structural determinations. Despite a rotation (indicated by red arrows) of the central domains, the pore of ATP, caffeine and Ca^{2+}-activated RyR2 channel remains open in the presence of Ca^{2+}-CaM under these two conditions (left four). By contrast, Ca^{2+}-CaM leads to closure of PCB95 and Ca^{2+}-activated RyR2 channel (right two). Our study demonstrates that the inhibitory force of Ca^{2+}-CaM can overcome the synergistic activation by PCB95 and Ca^{2+} but not by ATP, caffeine and Ca^{2+} (bottom right). The top right structure PCB95/low-Ca^{2+} was obtained from a previous study (RCSB Protein Data Bank (PDB) code 5GOA).

Discussion

Among the reported RyR2 sequences for CaM-binding[38], residues 4247–4277 are invisible in our structure. The segment (residues 2023–2039) that contains the protein kinase A phosphorylation site Ser2032 is resolved in our structures, but shows no interaction with CaM even at high concentrations[39]. The other two sequences (1942–1966 and 3582–3608) bind to CaM in our structures (Extended Data Fig. 10d). Despite the distinct effects of apo-CaM on RyR1 and RyR2[14], the primary apo-CaM-binding sequences are invariant in these two isoforms (Extended Data Fig. 10e). The molecular determinants for the functional difference are yet to be revealed.

The inhibitory mechanisms by which CaM regulates RyR2 must be investigated on an already opened channel by structural biology. As the presence of micromolar-range Ca^{2+} is required for opening ryanodine receptors by cryo-EM studies[30–32,37], it is impractical to obtain an open structure in the absence of micromolar concentrations of Ca^{2+} (apo-CaM form). Although the location and conformation of CaM-M appear identical to those of apo-CaM, it has previously been reported that modulation of RyR2 by CaM-M is distinct from that by apo-CaM[40]—although the mechanism needs to be investigated further.

Owing to extensive interactions between the U-motif and O-ring, the two undergo coupled motions during channel gating[30,37]. The presence of caffeine and ATP locks them into a more rigid structure, probably increasing the energy barrier for inhibiting RyR2 by Ca^{2+}-CaM. By contrast, the PCB95- and Ca^{2+}-activated RyR2 channel can be effectively closed by Ca^{2+}-CaM. Therefore, the gating state of RyR2 is defined by the combined effect of competing stimulatory and inhibitory regulators (Fig. 4). It remains to be investigated whether the conclusions presented here can be recapitulated for other ryanodine receptor isoforms or in lipid bilayers and the relevance to disease-related mutations (Extended Data Fig. 10f, g).

Online content

Any methods, additional references, Nature Research reporting summaries, source data, extended data, supplementary information, acknowledgements, peer review information; details of author contributions and competing interests; and statements of data and code availability are available at https://doi.org/10.1038/s41586-019-1377-y.

Received: 26 January 2019; Accepted: 4 June 2019;
Published online 5 July 2019.

1. Fabiato, A. Calcium-induced release of calcium from the cardiac sarcoplasmic reticulum. *Am. J. Physiol.* **245**, C1–C14 (1983).
2. Nakai, J. et al. Primary structure and functional expression from cDNA of the cardiac ryanodine receptor/calcium release channel. *FEBS Lett.* **271**, 169–177 (1990).
3. Otsu, K. et al. Molecular cloning of cDNA encoding the Ca^{2+} release channel (ryanodine receptor) of rabbit cardiac muscle sarcoplasmic reticulum. *J. Biol. Chem.* **265**, 13472–13483 (1990).
4. Rodney, G. G., Williams, B. Y., Strasburg, G. M., Beckingham, K. & Hamilton, S. L. Regulation of RYR1 activity by Ca^{2+} and calmodulin. *Biochemistry* **39**, 7807–7812 (2000).
5. Timerman, A. P. et al. The ryanodine receptor from canine heart sarcoplasmic reticulum is associated with a novel FK-506 binding protein. *Biochem. Biophys. Res. Commun.* **198**, 701–706 (1994).
6. Yamaguchi, N., Xu, L., Pasek, D. A., Evans, K. E. & Meissner, G. Molecular basis of calmodulin binding to cardiac muscle Ca^{2+} release channel (ryanodine receptor). *J. Biol. Chem.* **278**, 23480–23486 (2003).
7. Laitinen, P. J. et al. Mutations of the cardiac ryanodine receptor (RyR2) gene in familial polymorphic ventricular tachycardia. *Circulation* **103**, 485–490 (2001).
8. Medeiros-Domingo, A. et al. The *RYR2*-encoded ryanodine receptor/calcium release channel in patients diagnosed previously with either catecholaminergic polymorphic ventricular tachycardia or genotype negative, exercise-induced long QT syndrome: a comprehensive open reading frame mutational analysis. *J. Am. Coll. Cardiol.* **54**, 2065–2074 (2009).
9. Priori, S. G. & Chen, S. R. Inherited dysfunction of sarcoplasmic reticulum Ca^{2+} handling and arrhythmogenesis. *Circ. Res.* **108**, 871–883 (2011).
10. Priori, S. G. et al. Mutations in the cardiac ryanodine receptor gene (*hRyR2*) underlie catecholaminergic polymorphic ventricular tachycardia. *Circulation* **103**, 196–200 (2001).
11. Hoeflich, K. P. & Ikura, M. Calmodulin in action: diversity in target recognition and activation mechanisms. *Cell* **108**, 739–742 (2002).
12. Babu, Y. S. et al. Three-dimensional structure of calmodulin. *Nature* **315**, 37–40 (1985).
13. Copley, R. R., Schultz, J., Ponting, C. P. & Bork, P. Protein families in multicellular organisms. *Curr. Opin. Struct. Biol.* **9**, 408–415 (1999).
14. Balshaw, D. M., Xu, L., Yamaguchi, N., Pasek, D. A. & Meissner, G. Calmodulin binding and inhibition of cardiac muscle calcium release channel (ryanodine receptor). *J. Biol. Chem.* **276**, 20144–20153 (2001).
15. Moore, C. P. et al. Apocalmodulin and Ca^{2+} calmodulin bind to the same region on the skeletal muscle Ca^{2+} release channel. *Biochemistry* **38**, 8532–8537 (1999).
16. Tripathy, A., Xu, L., Mann, G. & Meissner, G. Calmodulin activation and inhibition of skeletal muscle Ca^{2+} release channel (ryanodine receptor). *Biophys. J.* **69**, 106–119 (1995).
17. Fruen, B. R., Bardy, J. M., Byrem, T. M., Strasburg, G. M. & Louis, C. F. Differential Ca^{2+} sensitivity of skeletal and cardiac muscle ryanodine receptors in the presence of calmodulin. *Am. J. Physiol. Cell Physiol.* **279**, C724–C733 (2000).
18. Tian, X., Tang, Y., Liu, Y., Wang, R. & Chen, S. R. Calmodulin modulates the termination threshold for cardiac ryanodine receptor-mediated Ca^{2+} release. *Biochem. J.* **455**, 367–375 (2013).
19. Hino, A. et al. Enhanced binding of calmodulin to the ryanodine receptor corrects contractile dysfunction in failing hearts. *Cardiovasc. Res.* **96**, 433–443 (2012).
20. Lavorato, M. et al. Dyad content is reduced in cardiac myocytes of mice with impaired calmodulin regulation of RyR2. *J. Muscle Res. Cell Motil.* **36**, 205–214 (2015).
21. Yamaguchi, N. et al. Cardiac hypertrophy associated with impaired regulation of cardiac ryanodine receptor by calmodulin and S100A1. *Am. J. Physiol. Heart Circ. Physiol.* **305**, H86–H94 (2013).
22. Yamaguchi, N., Takahashi, N., Xu, L., Smithies, O. & Meissner, G. Early cardiac hypertrophy in mice with impaired calmodulin regulation of cardiac muscle Ca release channel. *J. Clin. Invest.* **117**, 1344–1353 (2007).
23. Kato, T. et al. Correction of impaired calmodulin binding to RyR2 as a novel therapy for lethal arrhythmia in the pressure-overloaded heart failure. *Heart Rhythm* **14**, 120–127 (2017).
24. Huang, X., Fruen, B., Farrington, D. T., Wagenknecht, T. & Liu, Z. Calmodulin-binding locations on the skeletal and cardiac ryanodine receptors. *J. Biol. Chem.* **287**, 30328–30335 (2012).
25. Samsó, M. & Wagenknecht, T. Apocalmodulin and Ca^{2+}-calmodulin bind to neighboring locations on the ryanodine receptor. *J. Biol. Chem.* **277**, 1349–1353 (2002).
26. Wagenknecht, T. et al. Locations of calmodulin and FK506-binding protein on the three-dimensional architecture of the skeletal muscle ryanodine receptor. *J. Biol. Chem.* **272**, 32463–32471 (1997).
27. Yamaguchi, N., Xin, C. & Meissner, G. Identification of apocalmodulin and Ca^{2+}-calmodulin regulatory domain in skeletal muscle Ca^{2+} release channel, ryanodine receptor. *J. Biol. Chem.* **276**, 22579–22585 (2001).
28. Maximciuc, A. A., Putkey, J. A., Shamoo, Y. & Mackenzie, K. R. Complex of calmodulin with a ryanodine receptor target reveals a novel, flexible binding mode. *Structure* **14**, 1547–1556 (2006).
29. Maune, J. F., Klee, C. B. & Beckingham, K. Ca^{2+} binding and conformational change in two series of point mutations to the individual Ca^{2+}-binding sites of calmodulin. *J. Biol. Chem.* **267**, 5286–5295 (1992).
30. Peng, W. et al. Structural basis for the gating mechanism of the type 2 ryanodine receptor RyR2. *Science* **354**, aah5324 (2016).
31. des Georges, A. et al. Structural basis for gating and activation of RyR1. *Cell* **167**, 145–157 (2016).
32. Wei, R. et al. Structural insights into Ca^{2+}-activated long-range allosteric channel gating of RyR1. *Cell Res.* **26**, 977–994 (2016).
33. Wang, C. et al. Structural analyses of Ca^{2+}/CaM interaction with NaV channel C-termini reveal mechanisms of calcium-dependent regulation. *Nat. Commun.* **5**, 4896 (2014).
34. Wang, C., Chung, B. C., Yan, H., Lee, S. Y. & Pitt, G. S. Crystal structure of the ternary complex of a NaV C-terminal domain, a fibroblast growth factor homologous factor, and calmodulin. *Structure* **20**, 1167–1176 (2012).
35. Jurado, L. A., Chockalingam, P. S. & Jarrett, H. W. Apocalmodulin. *Physiol. Rev.* **79**, 661–682 (1999).
36. Rodney, G. G. et al. Calcium binding to calmodulin leads to an N-terminal shift in its binding site on the ryanodine receptor. *J. Biol. Chem.* **276**, 2069–2074 (2001).
37. Bai, X. C., Yan, Z., Wu, J., Li, Z. & Yan, N. The central domain of RyR1 is the transducer for long-range allosteric gating of channel opening. *Cell Res.* **26**, 995–1006 (2016).
38. Brohus, M., Søndergaard, M. T., Chen, S. R. W., van Petegem, F. & Overgaard, M. T. Ca^{2+}-dependent calmodulin binding to cardiac ryanodine receptor (RyR2) calmodulin-binding domains. *Biochem. J.* **476**, 193–209 (2019).
39. Xiao, B. et al. Characterization of a novel PKA phosphorylation site, serine-2030, reveals no PKA hyperphosphorylation of the cardiac ryanodine receptor in canine heart failure. *Circ. Res.* **96**, 847–855 (2005).
40. Fruen, B. R. et al. Regulation of the RYR1 and RYR2 Ca^{2+} release channel isoforms by Ca^{2+}-insensitive mutants of calmodulin. *Biochemistry* **42**, 2740–2747 (2003).
41. Smart, O. S., Neduvelil, J. G., Wang, X., Wallace, B. A. & Sansom, M. S. HOLE: a program for the analysis of the pore dimensions of ion channel structural models. *J. Mol. Graph.* **14**, 354–360 (1996).

METHODS

Expression and purification of GST–FKBP12.6. Because the sequence of porcine FKBP12.6 is not available in the public domain, human FKBP12.6 was applied to pull-down porcine RyR2 (pRyR2)[30]. The complementary DNA of full-length human *FKBP12.6* (also known as *FKBP1B*) was cloned into the pGEX-4T-2 vector with a C-terminal 6×His tag and an N-terminal glutathione *S*-transferase (GST) tag. Protein was overexpressed in the *Escherichia coli* BL21 (DE3) strain at 18 °C for 12–15 h after the addition of 0.2 mM isopropyl-β-D-thiogalactoside (IPTG) to cells with an optical density at 600 nm (OD_{600}) of 1.0. Cells collected by centrifugation were resuspended in lysis buffer (25 mM Tris, pH 8.0, 150 mM NaCl). Cell debris was removed by centrifugation at 22,000*g* for 1 h, and the supernatant was applied to Ni^{2+}-NTA resin (Qiagen). The resin was washed with both W1 buffer (25 mM Tris, pH 8.0, 500 mM NaCl) and W2 buffer (25 mM Tris, pH 8.0, 20 mM imidazole) and eluted with 25 mM Tris, pH 8.0 and 300 mM imidazole. The elution was further purified by anion-exchange chromatography (SOURCE 15Q, GE Healthcare).

Expression and purification of the wild-type CaM and CaM mutant. In mammals, three independent genes (*CALM1*–*CALM3*) with approximately 80% identity[42] are transcribed into at least eight mRNAs that encode identical CaM proteins[43]. It has previously been reported that the first methionine residue of CaM was removed under physiological conditions[44]. The complementary DNA of human *CALM3* without the initial Met was cloned into the pET21 vector with an N-terminal 6×His tag followed by an N-terminal SUMO tag and a stop codon in the C terminus, preventing the translation of a C-terminal 6×His tag in the original pET21 vector (Extended Data Fig. 1a). The expression and purification protocol was similar to that of GST–FKBP12.6 mentioned above. Specifically, the N-terminal 6×His tag and SUMO tag were removed together by the SUMO protease Ulp1p[45] during purification. The CaM protein was further purified by anion-exchange chromatography (SOURCE 15Q, GE Healthcare) using buffer 1 (25 mM Tris, pH 8.0) and buffer 2 (1 M NaCl, 25 mM Tris, pH 8.0). Finally, the protein was applied to size-exclusion chromatography (SEC; Superdex-200, GE Healthcare) in buffer F (20 mM HEPES, pH 7.4, 200 mM NaCl, 0.1% digitonin, 1.3 μg ml^{-1} aprotinin, 1 μg ml^{-1} pepstatin, 5 μg ml^{-1} leupeptin, 0.2 mM PMSF and 2 mM DTT), which is the same as that used for the last-step purification of RyR2. The N-terminal boundary of wild-type CaM was confirmed by N-terminal sequencing (Extended Data Fig. 1b). The expression and purification of the CaM mutant that is deficient in Ca^{2+} binding at all four EF-hand Ca^{2+}-binding sites (E32A, E68A, E105A and E141A) (denoted as CaM-M) were the same as for the wild-type CaM.

Preparation of sarcoplasmic reticulum membranes from porcine heart. The procedures for preparing the membranes of the sarcoplasmic reticulum from porcine hearts were similar to previously described procedures[30]. A single porcine heart was cut into small pieces and then resuspended in five volumes of homogenization buffer A (20 mM HEPES, pH 7.4, 150 mM NaCl, 5 mM EDTA, 1.3 μg ml^{-1} aprotinin, 1 μg ml^{-1} pepstatin, 5 μg ml^{-1} leupeptin and 0.2 mM PMSF). Homogenization was performed in a blender (JYL-C010, Joyoung) for fifteen cycles. The debris was removed by low-speed centrifugation (6,000*g*) for 10 min. The supernatant was further centrifuged at high speed (20,000*g*) for 1 h. The pellet was then resuspended in two volumes of homogenization buffer B (20 mM HEPES, pH 7.4, 1 M NaCl, 1.3 μg ml^{-1} aprotinin, 1 μg ml^{-1} pepstatin, 5 μg ml^{-1} leupeptin, 0.2 mM PMSF and 2 mM DTT) and flash-frozen in liquid nitrogen.

Purification of pRyR2 by GST–FKBP12.6. The pRyR2–FKBP12.6 complex was purified based on previously described procedures[30] with slight modifications. The membrane of the sarcoplasmic reticulum from a single porcine heart was solubilized at 4 °C for 2 h in homogenization buffer B supplemented with 5% CHAPS and 1.25% soy bean lecithin. After solubilization, the final concentration of NaCl in the system was diluted to 200 mM by homogenization buffer B without NaCl. Approximately 5–6 mg of purified GST–FKBP12.6 was then added to the system and further incubated for 1 h at 4 °C. After ultrahigh-speed centrifugation (200,000*g*), the supernatant was loaded onto a GS4B column (GE Healthcare). The resin was washed with buffer similar to the homogenization buffer B, except that the NaCl concentration was 200 mM and 0.1% digitonin was added. The complex was eluted by a solution containing 80 mM Tris, pH 8.0, 200 mM NaCl, 10 mM GSH, 0.1% digitonin, 1.3 μg ml^{-1} aprotinin, 1 μg ml^{-1} pepstatin, 5 μg ml^{-1} leupeptin, 0.2 mM PMSF and 2 mM DTT. The eluted protein was further purified through SEC (Superose 6, 10/300 GL, GE Healthcare) in buffer F. The pRyR2–FKBP12.6 complex fractions were concentrated to approximately 0.1 mg ml^{-1} for electron microscopy sample preparation. Specifically, for the FKBP12.6/apo-CaM sample, 5 mM EDTA, which has no effect on the zinc finger structure of RyR2[30], was included throughout purification of RyR2. For the CHAPS- and DOPC-treated FKBP12.6/ATP/caffeine/low-[Ca^{2+}] and CHAPS- and DOPC-treated FKBP12.6/ATP/caffeine/low-[Ca^{2+}]/Ca^{2+}-CaM samples, the proteins were extracted only by CHAPS and washed and eluted by a buffer containing 0.5% CHAPS plus 0.002% DOPC. The eluted proteins were further purified through SEC in buffer F except 0.1% digitonin was replaced by 0.25% CHAPS plus 0.001% DOPC. For the PCB95/low-[Ca^{2+}]/Ca^{2+}-CaM sample, the proteins were purified using GST–FKBP12 as a bait and the RyR2–FKBP12 (containing GST–FKBP12) complex fell apart during SEC purification[30].

Cryo-EM sample preparation. The cryo-EM samples of RyR2–CaM complexes were prepared as follows. FKBP12.6/apo-CaM: 5 mM EDTA was added to CaM (in buffer F) before sample preparation, and CaM with a final concentration of 250 μM was added to RyR2 (in buffer F plus 5 mM EDTA). FKBP12.6/ATP/caffeine/low-[Ca^{2+}]/CaM-M: CaM-M (in buffer F) and RyR2 (in buffer F) were separately added with 20 μM Ca^{2+} (low-Ca^{2+} concentration), 5 mM ATP and 5 mM caffeine and CaM-M with a final concentration of 250 μM was added to RyR2. FKBP12.6/ATP/caffeine/low-[Ca^{2+}]/Ca^{2+}-CaM: CaM (in buffer F) and RyR2 (in buffer F) were separately added to 20 μM Ca^{2+}, 5 mM ATP and 5 mM caffeine and CaM with a final concentration of 2.5 μM was added to RyR2. The other samples were prepared by the same procedure. Note that 5 mM Ca^{2+} represents high-Ca^{2+} concentration. Vitrobot Mark IV (FEI) was used for the preparation of cryo-EM grids. The procedures for preparing the eight samples were the same. Aliquots (3 μl each) of pRyR2 samples were placed on glow-discharged lacey carbon grids (Ted Pella). Grids were blotted for 2 s and flash-frozen in liquid ethane. Owing to the presence of high concentrations of Ca^{2+} in the filter paper used for blotting, it has previously been reported that the final concentration of free Ca^{2+} may be much higher than those used during sample preparation[46]. The low- and high-Ca^{2+} concentrations presented here only indicate those used during sample preparation and may be lower than the true Ca^{2+} concentrations.

Cryo-EM image acquisition. With regard to the FKBP12.6/ATP/caffeine/low-[Ca^{2+}], FKBP12.6/ATP/caffeine/low-[Ca^{2+}]/CaM-M, CHAPS- and DOPC-treated FKBP12.6/ATP/caffeine/low-[Ca^{2+}], CHAPS- and DOPC-treated FKBP12.6/ATP/caffeine/low-[Ca^{2+}]/Ca^{2+}-CaM, FKBP12.6/ATP/caffeine/high-[Ca^{2+}]/Ca^{2+}-CaM and PCB95/low-[Ca^{2+}]/Ca^{2+}-CaM datasets, grids were transferred to a Titan Krios (Thermo Fisher Scientific) electron microscope operating at 300 kV equipped with a Cs-corrector (Thermo Fisher Scientific), Gatan K2 Summit detector and GIF Quantum energy filter. Zero-loss movie stacks were automatically collected using AutoEMationII[47,48] with a slit width of 20 eV on the energy filter and a defocus range from −1.3 μm to −1.7 μm in super-resolution mode at a nominal magnification of 105,000×. Each stack was exposed for 5.6 s with an exposure time of 0.175 s per frame, resulting in 32 frames per stack. The total dose was approximately 50 e^{-} $Å^{-2}$ for each stack. The stacks were motion-corrected with MotionCor2[49] and binned twofold, resulting in a pixel size of 1.091 Å per pixel. With regard to the FKBP12.6/apo-CaM and FKBP12.6/ATP/caffeine/low-[Ca^{2+}]/Ca^{2+}-CaM datasets, micrographs were collected using a Gatan K2 Summit detector mounted on a Titan Krios electron microscope (FEI Company) operating at 300 kV and equipped with a GIF Quantum energy filter (slit width 20 eV). Micrographs were recorded in the super-resolution mode with a normal magnification of 105,000 ×, resulting in a calibrated pixel size of 0.669 Å. Each stack of 32 frames was exposed for 8 s, with an exposing time of 0.25 s per frame. The total dose rate was about 45.6 e^{-} $Å^{-2}$ for each stack. All 32 frames in each stack were motion-corrected with MotionCor2 and binned to a pixel size of 1.338 Å. The defocus value of each image was set from −0.8 μm to −1.8 μm. In addition, dose weighting was performed[50]. The defocus values were estimated with Gctf[51].

Image processing. Image-processing procedures were similar to those previously reported[30]. Diagrams of the procedures used in data processing are presented in Extended Data Fig. 2. For the FKBP12.6/apo-CaM dataset, 1,180,104 particles were picked from 7,800 micrographs by RELION 2.0[52] using templates low-pass-filtered to 20 Å to limit reference bias. After two rounds of two-dimensional classification, 832,833 particles were selected and subjected to global angular search three-dimensional classification using RELION 2.0 with one class and a step size of 7.5°. The electron microscopy map of the previously published open structure of RyR2[30], which was low-pass-filtered to 60 Å, was used as the initial model. After global angular search three-dimensional classification, the particles were further subjected to three-dimensional classification with 10 classes and a local angular search step of 3.75°. The local angular search three-dimensional classification was performed several times with the output from different iterations of the global angular search three-dimensional classification as input. After the merging of all good classes and removal of the duplicated particles, the particles were subjected to three-dimensional autorefinement using THUNDER software[53]. The final particle number for the three-dimensional autorefinement was 208,715, resulting in a 3.6 Å resolution map after post-processing. The same procedures were performed for the other datasets. The resolution was estimated with the gold-standard Fourier shell correlation 0.143 criterion[54] with the high-resolution noise-substitution method[55].

Model building and structure refinement. The model of the RyR2 open structure (PDB code 5GOA)[30] was fitted into the maps of the eight conditions by Chimera[56] and manually adjusted in COOT[57]. FKBP12 from the rabbit RyR1/FKBP12 complex structure (PDB code 3J8H)[58] was used for homologous model building of FKBP12.6. The apo-CaM from the crystal structure 3WFN was fitted into the maps obtained in the presence of CaM-M or apo-CaM and manually adjusted in

COOT. Similarly, the crystal structure of Ca^{2+}-CaM in complex with the RyR1 peptide (PDB code 2BCX) was fitted into the maps obtained in the presence of Ca^{2+}-CaM and manually adjusted in COOT. Structure refinement was performed using PHENIX[59] in real space with restrained secondary structure and geometry. The statistics of the three-dimensional reconstruction and model refinement are summarized in Extended Data Table 1.

Evaluation of the conformations of N- and C-lobes of CaM. Different conformations of N- and C-lobes were docked into the electron microscopy reconstruction for FKBP12.6/ATP/caffeine/high-[Ca^{2+}]/Ca^{2+}-CaM using the 'Fit in Map' tool of Chimera, selecting the options that include 'Real-time correlation', '7-Å resolution of Use map simulated from atoms', 'Use only data above contour level from first map', 'Optimize correlation', 'Correlation calculated about mean data value', 'Allow rotation and shift' and 'Move whole molecules'.

Site-directed mutagenesis. Point mutations in mouse *Ryr2* and in human *CALM1* were generated with the overlap extension method using PCR. In brief, a EcoRV/HpaI DNA fragment containing the RyR2(Y2156A) mutation and an AgeI/SalI fragment containing the RyR2(V3599A), RyR2(W3587A) or RyR2(L3590A) mutations were obtained by overlapping PCR and used to replace the corresponding wild-type fragment in the NheI/BsiWI fragment of *Ryr2*, The mutated NheI/BsiWI fragment was then used to replace the corresponding wild-type fragment in the full-length *Ryr2* cDNA in pcDNA5. A HindIII/XhoI full-length *CALM1* DNA fragment containing various point mutations was generated by overlapping PCR, which was then subcloned into pcDNA3. All point mutations in *Ryr2* and *CALM1* were confirmed by DNA sequencing.

Generation of stable, inducible cell lines expressing RyR2(WT) and mutants. Stable, inducible HEK293 cell lines expressing RyR2(WT), RyR2(Y2156A), RyR2(V3599A), RyR2(W3587A) and RyR2(L3590A) were generated using the Flp-In T-REx Core Kit from Invitrogen. These cell lines were not authenticated. These cells tested negative for mycoplasma contamination. In brief, Flp-In T-REx HEK293 cells were co-transfected with the inducible expression vector pcDNA5/FRT/TO containing the $Ryr2^{WT}$ or *Ryr2*-mutant cDNA and the pOG44 vector encoding the Flp recombinase in 1:5 ratios using the calcium phosphate precipitation method. The transfected cells were washed with phosphate buffered saline (PBS; 137 mM NaCl, 8 mM Na_2HPO_4, 1.5 mM KH_2PO_4 and 2.7 mM KCl, pH 7.4) 24 h after transfection followed by a change into fresh medium for 24 h. The cells were then washed again with PBS, collected and plated onto new dishes. After the cells had attached (around 4 h), the growth medium was replaced with a selection medium containing 200 μg ml^{-1} hygromycin (Invitrogen). The selection medium was changed every 3–4 days until the desired number of cells was grown. The hygromycin-resistant cells were pooled, aliquoted (1 ml) and stored at −80 °C. These positive cells are believed to be isogenic, because the integration of *Ryr2* cDNA is mediated by the Flp recombinase at a single FRT site.

Single-cell luminal Ca^{2+} imaging. Luminal Ca^{2+} levels in $Ryr2^{WT}$- or *Ryr2*-mutant-expressing HEK293 cells transfected with or without CaM(WT) or CaM mutants were measured using single-cell Ca^{2+} imaging and the fluorescence resonance energy transfer (FRET)-based endoplasmic-reticulum luminal Ca^{2+}-sensitive chameleon protein D1ER as previously described[60,61]. The cells were grown to 95% confluence in a 75-cm^2 flask, dissociated with PBS (137 mM NaCl, 8 mM Na_2HPO_4, 1.5 mM KH_2PO_4 and 2.7 mM KCl, pH 7.4) and plated on glass coverslips placed on tissue culture dishes at approximately 10% confluence 18–20 h before transfection with cDNA for D1ER and cDNAs for CaM(WT) or CaM mutants using the calcium phosphate precipitation method. After transfection for 24 h, the growth medium was then changed to an induction medium containing 1 μg ml^{-1} tetracycline. After induction for around 22 h, the coverslip was mounted onto an inverted microscope (Nikon TE2000-S) and the cells on the coverslip were perfused continuously with Krebs–Ringer–HEPES buffer (125 mM NaCl, 5 mM KCl, 1.2 mM KH_2PO_4, 6 mM glucose, 1.2 mM $MgCl_2$ and 25 mM HEPES, pH 7.4) containing various concentrations of $CaCl_2$ (0, 1 and 2 mM) to induce SOICR, followed by the addition of 1.0 mM tetracaine, which was used to estimate the store capacity, and caffeine (20 mM), which was used to estimate the minimum store level by depleting the endoplasmic-reticulum Ca^{2+} stores at room temperature (23 °C). Images were captured with Compix Simple PCI 6 software every 2 s using the Nikon TE2000-S inverted microscope equipped with an S-Fluor 20×/0.75 NA objective. The filters used for D1ER imaging were $\lambda_{ex} = 436 \pm 20$ nm for CFP and $\lambda_{ex} = 500 \pm 20$ nm for YFP, and $\lambda_{em} = 465 \pm 30$ nm for CFP and $\lambda_{em} = 535 \pm 30$ nm for YFP with a dichroic mirror (500 nm). The amount of FRET in individual cells was determined from the ratio of the light emission at 535 and 465 nm. F_{SOICR} is defined as the FRET level at which SOICR occurs, and F_{termi} is defined as the FRET level at which SOICR terminates. The maximum FRET signal F_{max} is defined as the FRET level after tetracaine treatment. The minimum FRET signal F_{min} is defined as the FRET level after caffeine treatment. The termination and activation thresholds of SOICR in individual cells were determined using the equations shown in Extended Data Fig. 7a. The store capacity is calculated by subtracting F_{min} from F_{max}. Individual data points represent the average measurements of around 10–30 cells from one coverslip in one set of experiment. The number of experiments and coverslips for each condition is used as the sample size for data analyses.

Single-channel recordings in planar lipid bilayers. Recombinant RyR2(WT) and mutant channels were purified from cell lysates prepared from HEK293 cells transfected with the $Ryr2^{WT}$ or *Ryr2*-mutant (Y2156A, V3599A, W3587A or L3590A) cDNA by sucrose density gradient centrifugation as previously described[62]. Heart phosphatidylethanolamine (50%) and brain phosphatidylserine (50%) (Avanti Polar Lipids), dissolved in chloroform, were combined and dried under nitrogen gas and resuspended in 30 μl of *n*-decane at a concentration of 12 mg lipid per ml. Bilayers were formed across a 250-μm hole in a Delrin partition separating two chambers. The *trans* chamber (800 μl) was connected to the head stage input of an Axopatch 200A amplifier (Axon Instruments). The *cis* chamber (1.2 ml) was held at virtual ground. A symmetrical solution containing 250 mM KCl and 25 mM HEPES, pH 7.4 was used for all recordings, unless indicated otherwise. A 4-μl aliquot (around 1 μg protein) of the sucrose density gradient-purified recombinant RyR2(WT) or mutant channels was added to the *cis* chamber. Spontaneous channel activity was always tested for sensitivity to EGTA and Ca^{2+}. The chamber to which the addition of EGTA inhibited the activity of the incorporated channel presumably corresponds to the cytosolic side of the Ca^{2+} release channel. The direction of single channel currents was always measured from the luminal to the cytosolic side of the channel, unless mentioned otherwise. Recordings were filtered at 2,500 Hz. Data analyses were carried out using the pCLAMP 8.1 software package (Axon Instruments). Free Ca^{2+} concentrations were calculated using a computer program that has previously been described[63].

Statistical analysis. Data are mean ± s.e.m., derived from independent samples or independent experiments. All experiments were performed with at least five biological replicates. The GraphPad Prism 8.1 software was used to test for differences between groups. We used Student's *t*-test (paired, two-tailed) or one-way ANOVA with a Dunnett's post hoc test. $P < 0.05$ was considered to be statistically significant.

Reporting summary. Further information on research design is available in the Nature Research Reporting Summary linked to this paper.

Data availability

Atomic coordinates and electron microscopy density maps of the following structures have been deposited in the PDB (http://www.rcsb.org) and the Electron Microscopy Data Bank (EMDB https://www.ebi.ac.uk/pdbe/emdb/). FKBP12.6/apo-CaM (PDB, 6JI8; EMDB, EMD-9833), FKBP12.6/ATP/caffeine/low-[Ca^{2+}]/CaM-M (PDB, 6JII; EMDB, EMD-9834), FKBP12.6/ATP/caffeine/low-[Ca^{2+}] (PDB, 6JI0; EMDB, EMD-9831), FKBP12.6/ATP/caffeine/low-[Ca^{2+}]/Ca^{2+}-CaM (PDB, 6JIU; EMDB, EMD-9836), CHAPS- and DOPC-treated FKBP12.6/ATP/caffeine/low-[Ca^{2+}] (PDB, 6JRR; EMDB, EMD-9879), CHAPS- and DOPC-treated FKBP12.6/ATP/caffeine/low-[Ca^{2+}]/Ca^{2+}-CaM (PDB, 6JRS; EMDB, EMD-9880), FKBP12.6/ATP/caffeine/high-[Ca^{2+}]/Ca^{2+}-CaM (PDB, 6JIY; EMDB, EMD-9837) and PCB95/low-[Ca^{2+}]/Ca^{2+}-CaM (PDB, 6JV2; EMDB: EMD-9889) complexes. Source Data for Fig. 2e, f and Extended Data Figs. 1c, 6f, 7d–h are available in the online version of the paper. All other data are available from the corresponding authors upon reasonable request.

42. Fischer, R. et al. Multiple divergent mRNAs code for a single human calmodulin. *J. Biol. Chem.* **263**, 17055–17062 (1988).
43. Kortvely, E. & Gulya, K. Calmodulin, and various ways to regulate its activity. *Life Sci.* **74**, 1065–1070 (2004).
44. Sasagawa, T. et al. Complete amino acid sequence of human brain calmodulin. *Biochemistry* **21**, 2565–2569 (1982).
45. Hirano, H., Kobayashi, J. & Matsuura, Y. Structures of the karyopherins Kap121p and Kap60p bound to the nuclear pore-targeting domain of the SUMO protease Ulp1p. *J. Mol. Biol.* **429**, 249–260 (2017).
46. Paknejad, N. & Hite, R. K. Structural basis for the regulation of inositol trisphosphate receptors by Ca^{2+} and IP_3. *Nat. Struct. Mol. Biol.* **25**, 660–668 (2018).
47. Fan, X. et al. Near-atomic resolution structure determination in over-focus with volta phase plate by Cs-corrected cryo-EM. *Structure* **25**, 1623–1630 (2017).
48. Lei, J. & Frank, J. Automated acquisition of cryo-electron micrographs for single particle reconstruction on an FEI Tecnai electron microscope. *J. Struct. Biol.* **150**, 69–80 (2005).
49. Zheng, S. Q. et al. MotionCor2: anisotropic correction of beam-induced motion for improved cryo-electron microscopy. *Nat. Methods* **14**, 331–332 (2017).
50. Grant, T. & Grigorieff, N. Measuring the optimal exposure for single particle cryo-EM using a 2.6 Å reconstruction of rotavirus VP6. *eLife* **4**, e06980 (2015).
51. Zhang, K. Gctf: real-time CTF determination and correction. *J. Struct. Biol.* **193**, 1–12 (2016).
52. Kimanius, D., Forsberg, B. O., Scheres, S. H. & Lindahl, E. Accelerated cryo-EM structure determination with parallelisation using GPUs in RELION-2. *eLife* **5**, e18722 (2016).
53. Hu, M. et al. A particle-filter framework for robust cryo-EM 3D reconstruction. *Nat. Methods* **15**, 1083–1089 (2018).

54. Rosenthal, P. B. & Henderson, R. Optimal determination of particle orientation, absolute hand, and contrast loss in single-particle electron cryomicroscopy. *J. Mol. Biol*. **333**, 721–745 (2003).
55. Chen, S. et al. High-resolution noise substitution to measure overfitting and validate resolution in 3D structure determination by single particle electron cryomicroscopy. *Ultramicroscopy* **135**, 24–35 (2013).
56. Pettersen, E. F. et al. UCSF Chimera—a visualization system for exploratory research and analysis. *J. Comput. Chem*. **25**, 1605–1612 (2004).
57. Emsley, P., Lohkamp, B., Scott, W. G. & Cowtan, K. Features and development of Coot. *Acta Crystallogr. D* **66**, 486–501 (2010).
58. Yan, Z. et al. Structure of the rabbit ryanodine receptor RyR1 at near-atomic resolution. *Nature* **517**, 50–55 (2015).
59. Adams, P. D. et al. PHENIX: a comprehensive Python-based system for macromolecular structure solution. *Acta Crystallogr. D* **66**, 213–221 (2010).
60. Palmer, A. E., Jin, C., Reed, J. C. & Tsien, R. Y. Bcl-2-mediated alterations in endoplasmic reticulum Ca^{2+} analyzed with an improved genetically encoded fluorescent sensor. *Proc. Natl Acad. Sci. USA* **101**, 17404–17409 (2004).
61. Jones, P. P. et al. Endoplasmic reticulum Ca^{2+} measurements reveal that the cardiac ryanodine receptor mutations linked to cardiac arrhythmia and sudden death alter the threshold for store-overload-induced Ca^{2+} release. *Biochem. J.* **412**, 171–178 (2008).
62. Jiang, D. et al. Enhanced store overload-induced Ca^{2+} release and channel sensitivity to luminal Ca^{2+} activation are common defects of RyR2 mutations linked to ventricular tachycardia and sudden death. *Circ. Res*. **97**, 1173–1181 (2005).
63. Fabiato, A. & Fabiato, F. Calculator programs for computing the composition of the solutions containing multiple metals and ligands used for experiments in skinned muscle cells. *J. Physiol*. **75**, 463–505 (1979).

Acknowledgements We thank X. Li for technical support for electron microscopy image acquisition; the Tsinghua University Branch of China National Center for Protein Sciences (Beijing) for providing the cryo-EM facility support; the computational facility support on the cluster of Bio-Computing Platform (Tsinghua University Branch of China National Center for Protein Sciences Beijing) and the 'Explorer 100' cluster system of Tsinghua National Laboratory for Information Science and Technology; M. T. Overgaard for providing the CaM protein for single channel studies. This work was funded by the National Key R&D Program (2016YFA0500402) and the National Key Basic Research (973) Program (2015CB910101) from Ministry of Science and Technology of China and the National Natural Science Foundation of China (projects 31621092, 31630017 and 81861138009). N.Y. is supported by the Shirley M. Tilghman endowed professorship from Princeton University. This work was also supported by research grants from the Heart and Stroke Foundation of Canada, the Canadian Institutes of Health Research and the Heart and Stroke Foundation Chair in Cardiovascular Research (S.R.W.C.).

Author contributions D.G. and N.Y. conceived the project. D.G., X.C. and G.Z. prepared the electron microscopy samples. D.G., X.C., G.H. and J.L. conducted the cryo-EM analysis. J.W., L.Z. and R.W. performed the functional experiments. All authors contributed to data analysis. D.G., S.R.W.C. and N.Y. wrote the manuscript.

Competing interests The authors declare no competing interests.

Additional information

Supplementary information is available for this paper at https://doi.org/10.1038/s41586-019-1377-y.

Correspondence and requests for materials should be addressed to D.G., S.R.W.C. or N.Y.

Peer review information *Nature* thanks Youxing Jiang, Filip Van Petegem and the other anonymous reviewer(s) for their contribution to the peer review of this work.

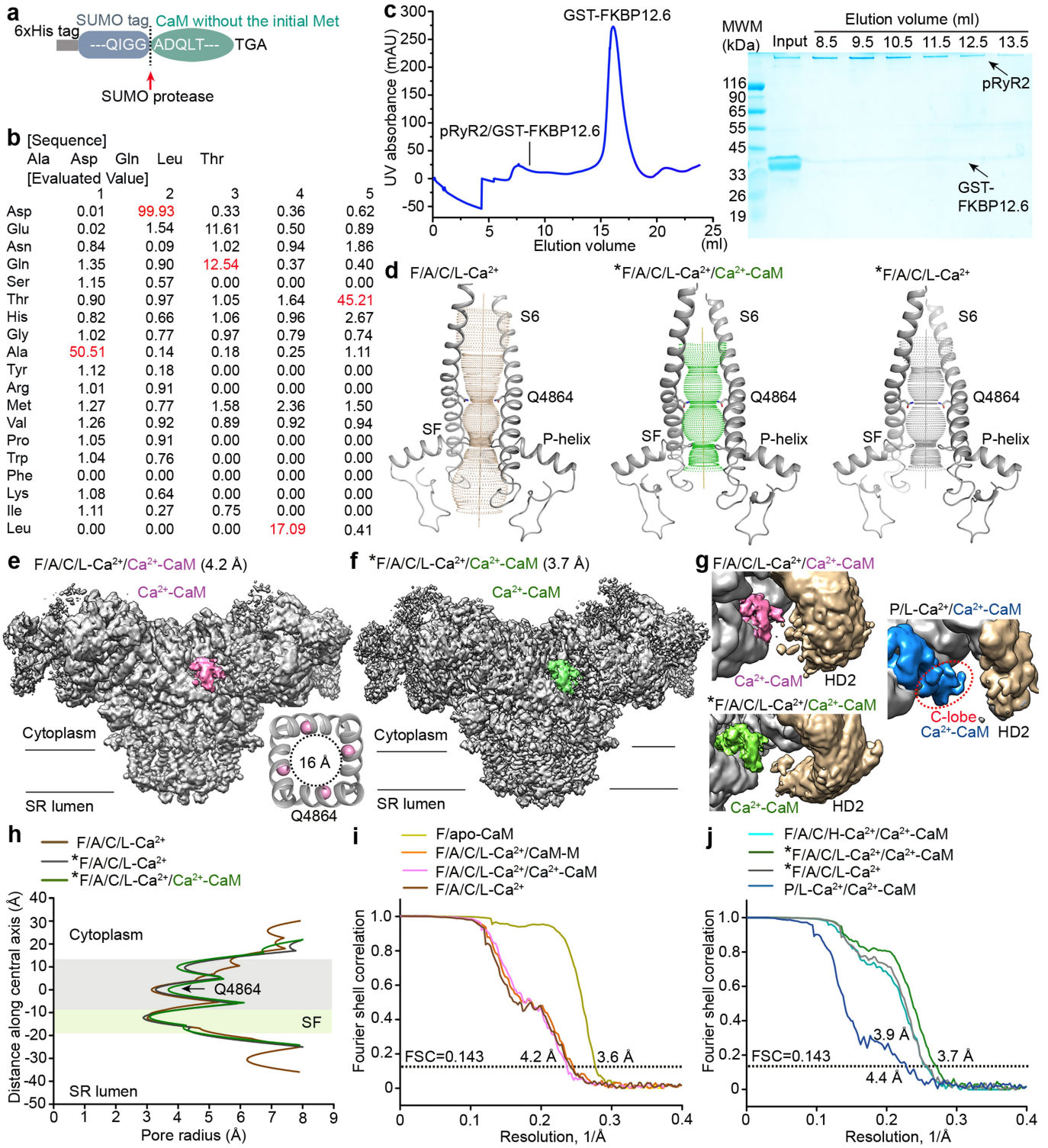

	1	2	3	4	5
Asp	0.01	99.93	0.33	0.36	0.62
Glu	0.02	1.54	11.61	0.50	0.89
Asn	0.84	0.09	1.02	0.94	1.86
Gln	1.35	0.90	12.54	0.37	0.40
Ser	1.15	0.57	0.00	0.00	0.00
Thr	0.90	0.97	1.05	1.64	45.21
His	0.82	0.66	1.06	0.96	2.67
Gly	1.02	0.77	0.97	0.79	0.74
Ala	50.51	0.14	0.18	0.25	1.11
Tyr	1.12	0.18	0.00	0.00	0.00
Arg	1.01	0.91	0.00	0.00	0.00
Met	1.27	0.77	1.58	2.36	1.50
Val	1.26	0.92	0.89	0.92	0.94
Pro	1.05	0.91	0.00	0.00	0.00
Trp	1.04	0.76	0.00	0.00	0.00
Phe	0.00	0.00	0.00	0.00	0.00
Lys	1.08	0.64	0.00	0.00	0.00
Ile	1.11	0.27	0.75	0.00	0.00
Leu	0.00	0.00	0.00	17.09	0.41

Extended Data Fig. 1 | See next page for caption.

Extended Data Fig. 1 | Protein purification and structural determination. a, Schematic of vector construction for recombinant expression of CaM without the N-terminal Met. **b**, N-terminal sequencing confirmed removal of the initial Met. **c**, SEC purification of the affinity-purified complex of pRyR2–FKBP12.6 (containing GST–FKBP12.6). The experiment was repeated five times independently with similar results. Peak fractions were resolved by SDS–PAGE and visualized by Coomassie blue staining (Supplementary Fig. 1). UV, ultraviolet. MWM, molecular weight marker. **d**, The channel is open in the presence of ATP, caffeine and Ca^{2+} under both digitonin and CHAPS-and-DOPC (indicated by an asterisk) conditions. The pore of CHAPS- and DOPC-treated FKBP12.6/ATP/caffeine/low-[Ca^{2+}]/Ca^{2+}-CaM remains open after Ca^{2+}-CaM loading. The ion-conduction path, calculated by HOLE, is illustrated by dots in each structure. A, ATP; C, caffeine; Ca^{2+}-CaM, Ca^{2+}-bound CaM; CaM-M, a Ca^{2+}-binding-deficient CaM mutant that mimics apo-CaM; F, FKBP12.6; L-Ca^{2+}, low Ca^{2+} concentration. **e**, Overall electron microscopy map of the FKBP12.6/ATP/caffeine/low-[Ca^{2+}]/Ca^{2+}-CaM complex. Inset, the cytoplasmic view of the channel gate. Because the side chains of the Gln4864-gating residues are not well-resolved, the distance between the C_α atoms of Gln4864 gating in the diagonal protomers is shown in the dashed circle. The density corresponding to CaM was generated from the map that was low-pass-filtered to 5.6 Å with a contour level of 0.015; the other regions were from the 4.2 Å map with a contour level of 0.023. **f**, Overall electron microscopy map of the CHAPS- and DOPC-treated FKBP12.6/ATP/caffeine/low-[Ca^{2+}]/Ca^{2+}-CaM complex. The density corresponding to CaM was generated from the map that was low-pass-filtered to 5.6 Å with a contour level of 0.013; the other regions were from the 3.7 Å map with a contour level of 0.021. **g**, Although the concentrations of Ca^{2+}-CaM are the same in these three conditions, only the N-lobe can be resolved in the FKBP12.6/ATP/caffeine/low-[Ca^{2+}]/Ca^{2+}-CaM and CHAPS- and DOPC-treated FKBP12.6/ATP/caffeine/low-[Ca^{2+}]/Ca^{2+}-CaM RyR2 structures. The reason may be that the HD2 in these two structures presents a steric hindrance for C-lobe binding. P, PCB95. **h**, The corresponding pore radii of the three structures are plotted. **i, j**, Gold-standard Fourier shell correlation curves for electron microscopy maps of the eight datasets. H-Ca^{2+}, high Ca^{2+} concentration.

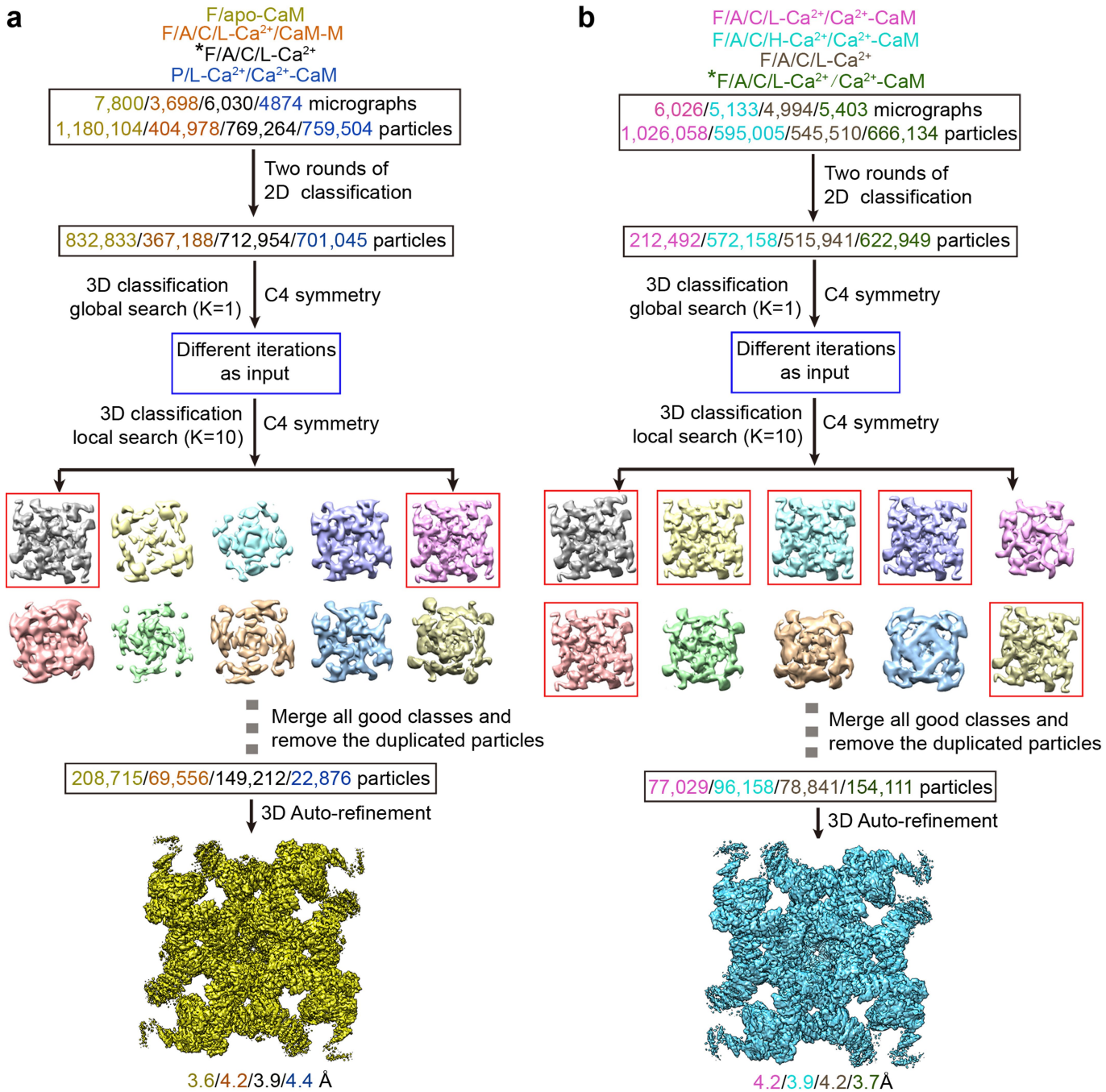

Extended Data Fig. 2 | Flow chart for cryo-EM data processing. See Methods for details. **a**, Data processing of the FKBP12.6/apoCaM, FKBP12.6/ATP/caffeine/low-[Ca^{2+}]/CaM-M, CHAPS- and DOPC-treated FKBP12.6/ATP/caffeine/low-[Ca^{2+}], and PCB95/low-[Ca^{2+}]/Ca^{2+}-CaM datasets. **b**, Data processing of the FKBP12.6/ATP/caffeine/low-[Ca^{2+}]/Ca^{2+}-CaM, FKBP12.6/ATP/caffeine/high-[Ca^{2+}]/Ca^{2+}-CaM, FKBP12.6/ATP/caffeine/low-[Ca^{2+}], and CHAPS- and DOPC-treated FKBP12.6/ATP/caffeine/low-[Ca^{2+}]/Ca^{2+}-CaM datasets.

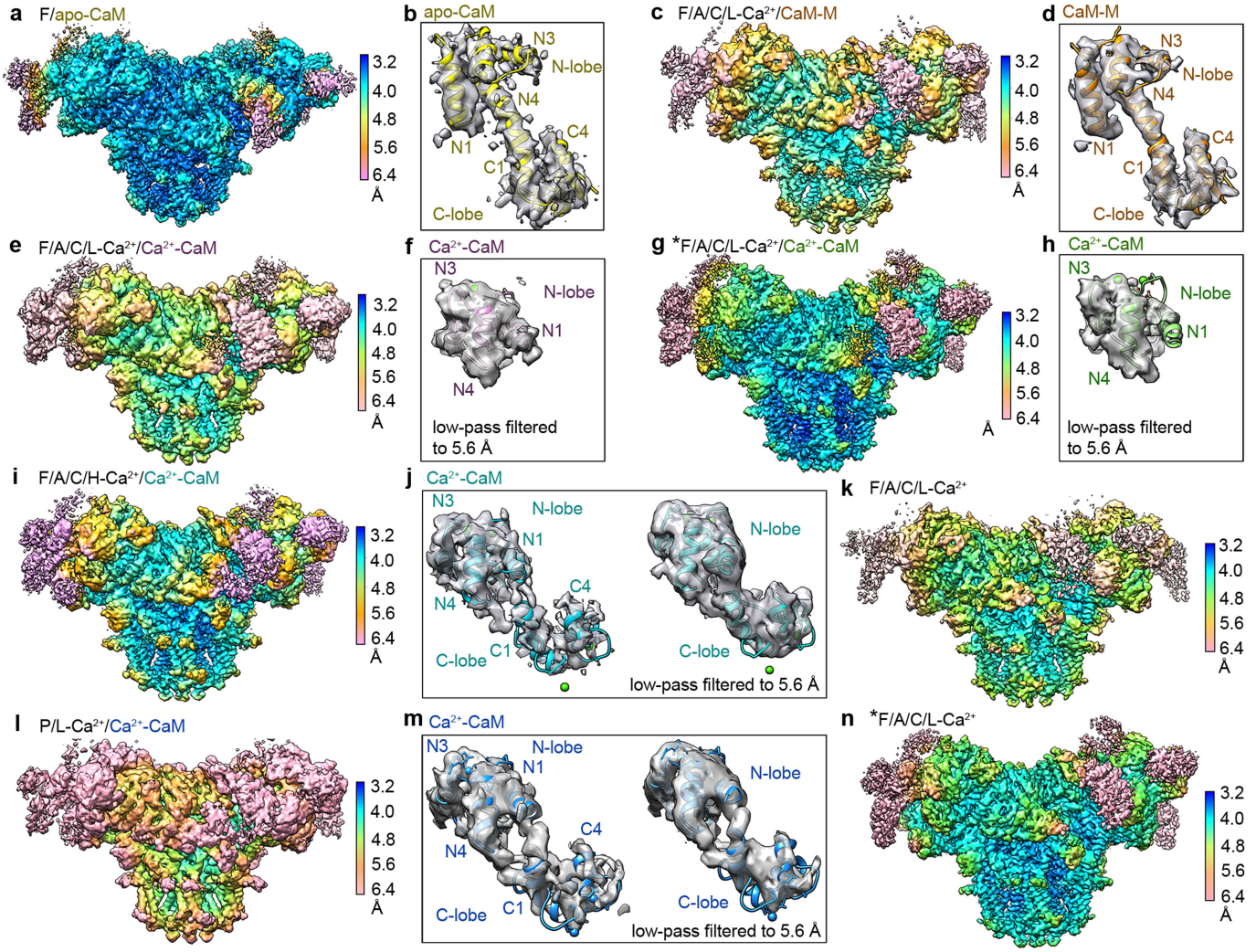

Extended Data Fig. 3 | Local resolution maps of the eight reconstructions. a, **c**, **e**, **g**, **i**, **k**, **l**, **n**, The local resolution maps estimated with RELION 2.0. All electron microscopy maps were generated in Chimera and contoured at levels of 0.027 (**a**), 0.022 (**c**), 0.023 (**e**), 0.021 (**g**), 0.02 (**i**), 0.021 (**k**), 0.015 (**l**) and 0.021 (**n**). **b**, Electron microscopy map of apo-CaM from the reconstruction shown in **a**. **d**, Electron microscopy map of CaM-M. **f**, **h**, The electron microscopy densities of Ca^{2+}-CaM were generated from the maps of FKBP12.6/ATP/caffeine/low-[Ca^{2+}]/Ca^{2+}-CaM and CHAPS- and DOPC-treated FKBP12.6/ATP/caffeine/low-[Ca^{2+}]/Ca^{2+}-CaM that were low-pass-filtered to 5.6 Å with contour levels of 0.015 (**f**) and 0.013 (**h**), respectively. **j**, **m**, Electron microscopy densities of Ca^{2+}-CaM in FKBP12.6/ATP/caffeine/high-[Ca^{2+}]/Ca^{2+}-CaM (**j**) and PCB95/low-[Ca^{2+}]/Ca^{2+}-CaM (**m**). The densities of both lobes were resolved in the map, although the N-lobe was resolved better than the C-lobe.

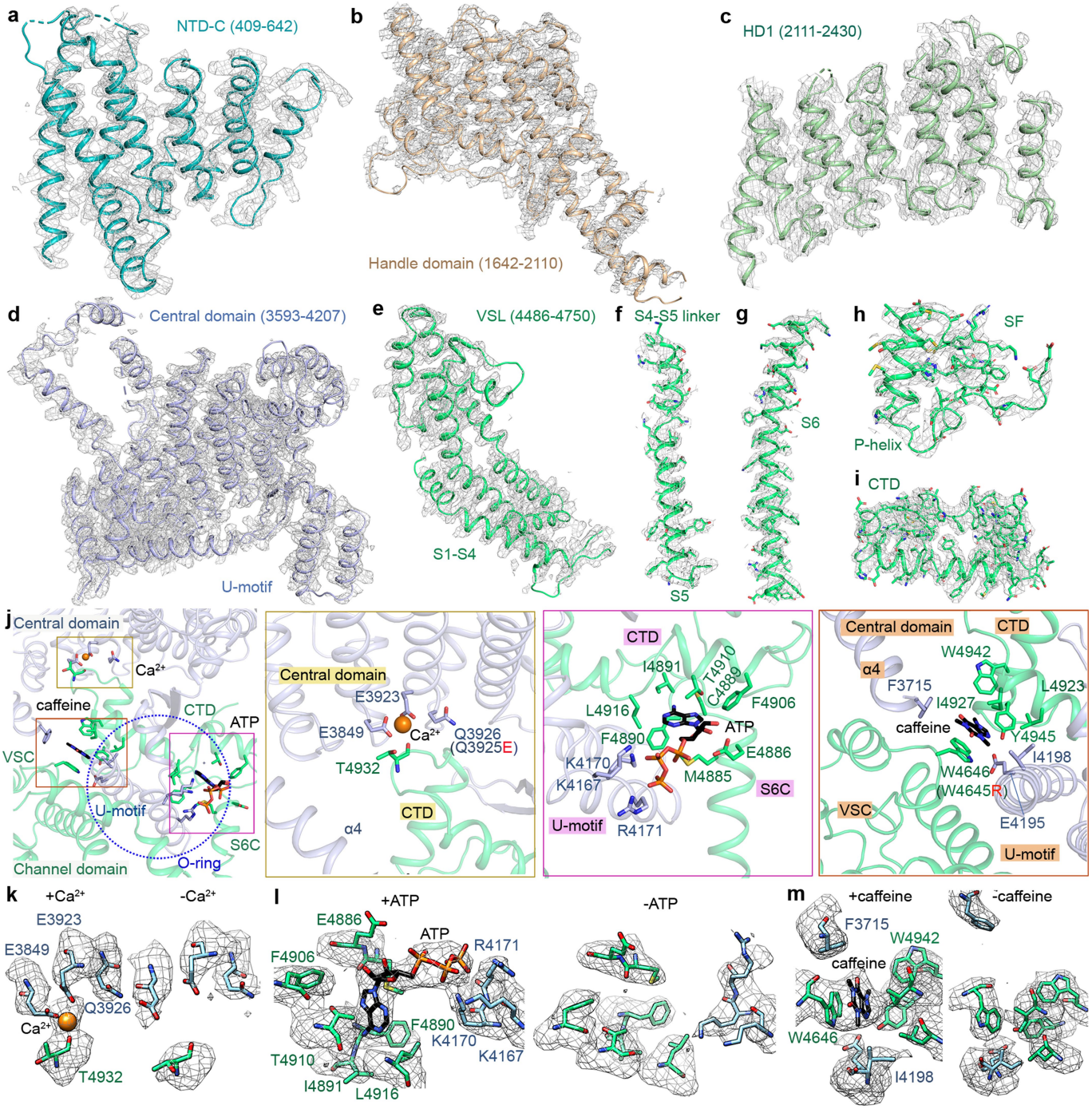

Extended Data Fig. 4 | Representative local electron microscopy maps for FKBP12.6/apo-CaM and densities of the binding sites for Ca^{2+}, ATP and caffeine in FKBP12.6/ATP/caffeine/high-[Ca^{2+}]/Ca^{2+}-CaM. a–i, The electron microscopy maps for the representative segments of RyR2. All of the maps were contoured at 5.5σ. **j,** The binding sites for Ca^{2+}, ATP and caffeine in RyR2. The blue, dotted circle indicates the O-ring that is formed by the C-terminal subdomain (CTD), cytoplasmic subdomain in the voltage-sensor-like domain (VSC) and the cytoplasmic portion of S6 (S6C). Ca^{2+} is located in the cleft that is formed by the central domain and C-terminal subdomain. ATP is located in a pocket formed by the U-motif, C-terminal subdomain and S6C. Caffeine is located at the interface formed by the U-motif, helix α4, C-terminal subdomain and voltage-sensor-like domain. The red letter indicates a disease-causing variant. **k–m,** The local densities of the Ca^{2+}-, ATP- and caffeine-binding sites. The electron microscopy maps of the FKBP12.6/ATP/caffeine/high-[Ca^{2+}]/Ca^{2+}-CaM (+ATP, caffeine and Ca^{2+}) and FKBP12.6/apo-CaM (−ATP, caffeine and Ca^{2+}) RyR2 structures are shown. All of the electron microscopy maps were contoured at a level of 0.029.

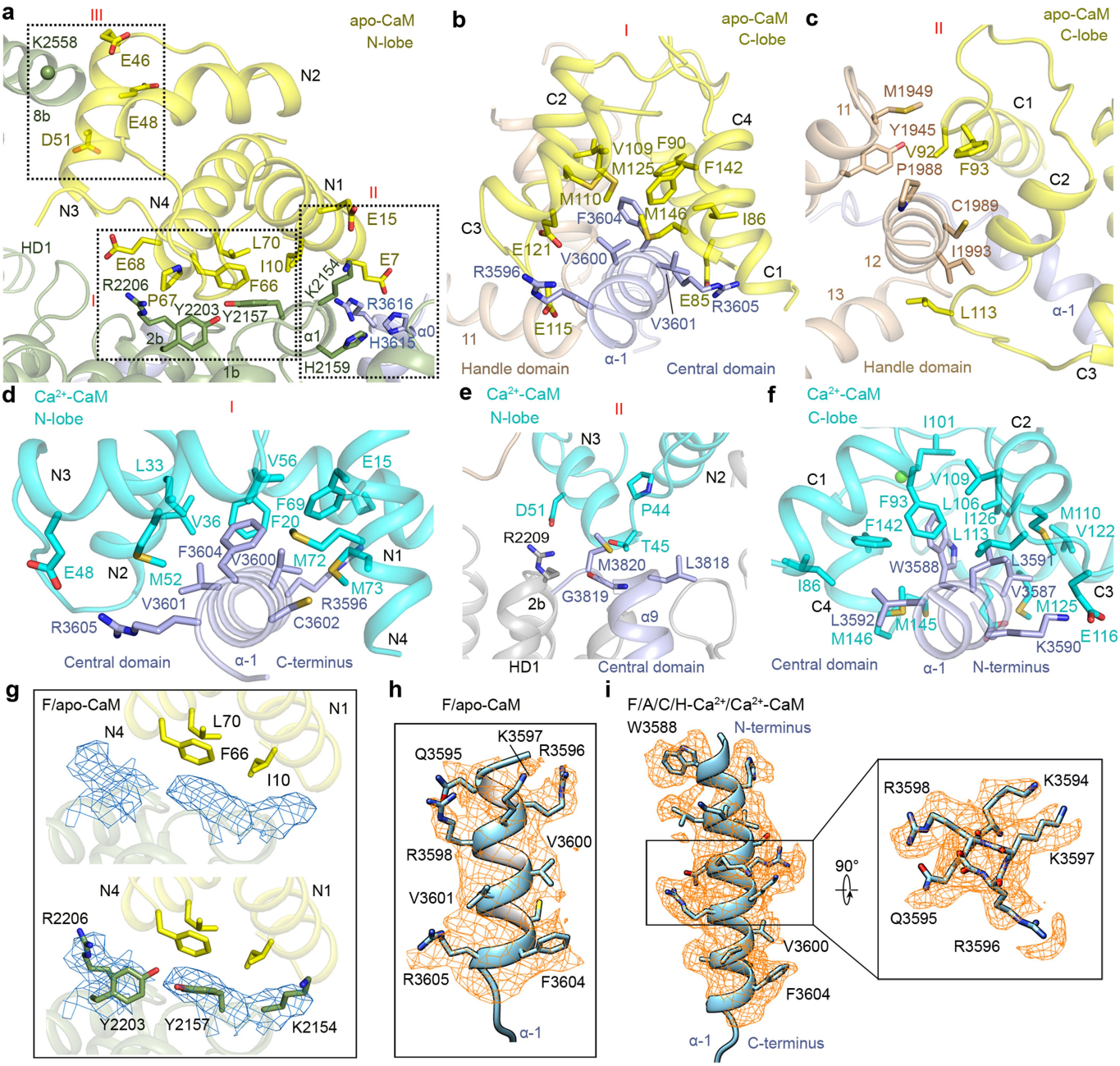

Extended Data Fig. 5 | Binding interfaces between CaM and RyR2. **a**, Three interfaces are formed between the N-lobe of apo-CaM and RyR2. HD1 serves as the major binding site for the N-lobe. The C_α atom of Lys2558 is shown as a sphere. **b**, **c**, Two interfaces are formed between the C-lobe of apo-CaM and RyR2. Helix α−1 is the major binding site of the C-lobe. **d**, **e**, The interfaces between the N-lobe of Ca^{2+}-CaM and RyR2. **f**, The interface between the C-lobe of Ca^{2+}-CaM and RyR2. **g**, Local densities of the probable interacting residues, Tyr2157, Tyr2203, Arg2206 and Lys2154 in RyR2. The electron microscopy map was contoured at 5.5σ. **h**, Density of helix α−1 in the FKBP12.6/apo-CaM RyR2 structure. The sequence can be reliably assigned based on the indicated bulky residues. **i**, Density of helix α−1 in the FKBP12.6/ATP/caffeine/high-[Ca^{2+}]/Ca^{2+}-CaM RyR2 structure. The C-terminal half of helix α−1 is reliably assigned, a few bulky residues facilitate the sequence alignment. As both the N-terminal half of helix α−1 and C-lobe of Ca^{2+}-CaM had a lower resolution, the density shown here may belong to Trp3588. The electron microscopy maps in **h** and **i** were contoured at levels of 0.027 and 0.016, respectively.

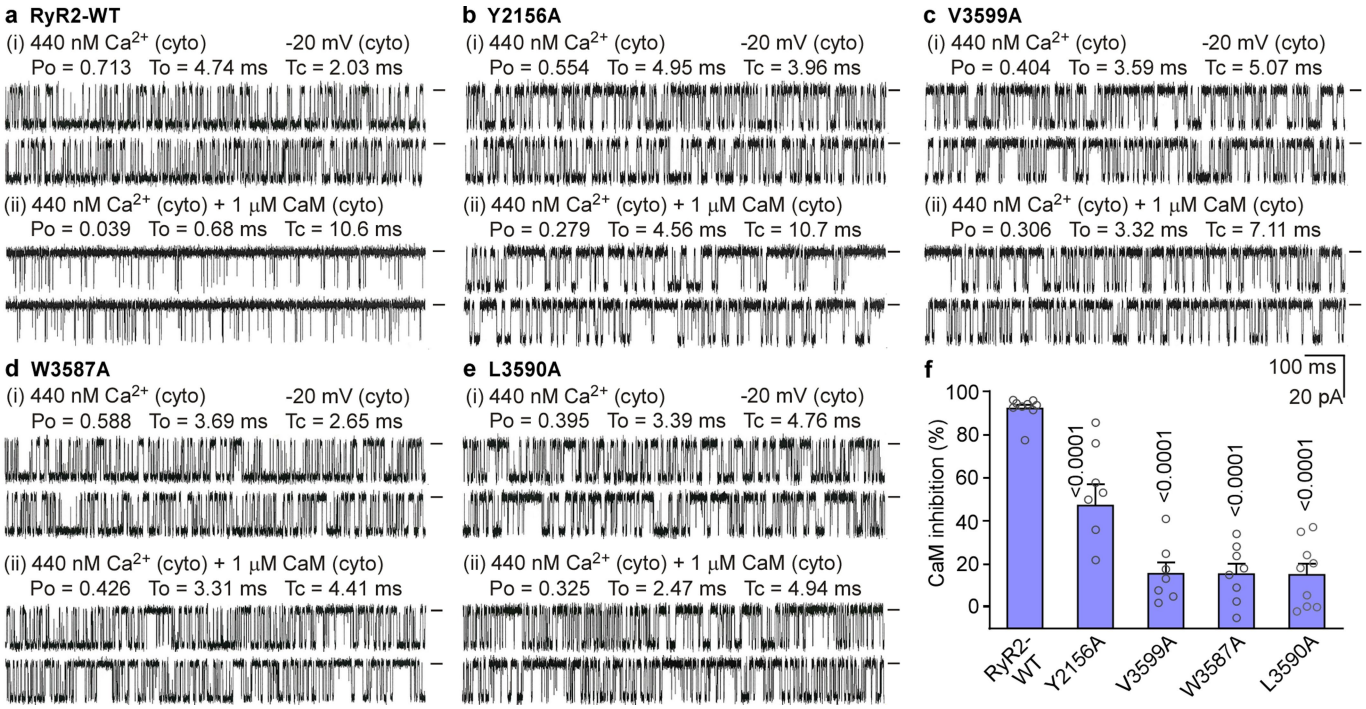

Extended Data Fig. 6 | Effect of RyR2 mutations on CaM regulation of single RyR2 channels. a–e, Single-channel activities were recorded in a symmetrical recording solution containing 250 mM KCl and 25 mM HEPES, pH 7.4. Representative current traces of single RyR2(WT) ($n = 9$), RyR2(Y2156A) ($n = 8$), RyR2(V3599A) ($n = 7$), RyR2(W3587A) ($n = 8$) and RyR2(L3590A) ($n = 9$) channels are shown. The Ca^{2+} concentration on the cytoplasmic and luminal face of the channel was 440 nM and around 45 nM, respectively. Open probability (Po), mean open time (To) and mean closed time (Tc) of the same channel before and after addition of CaM(WT) (1 μM) are depicted. Baselines are indicated by short bars on the right. **f**, Percentages of inhibition of channel open probability by CaM. Data are mean ± s.e.m. from single RyR2(WT) ($n = 9$), RyR2(Y2156A) ($n = 8$), RyR2(V3599A) ($n = 7$), RyR2(W3587A) ($n = 8$) and RyR2(L3590A) ($n = 9$) channels and analysed by one-way ANOVA with a Dunnett's post hoc test (versus RyR2(WT)) and adjusted *P* values are indicated on the graph.

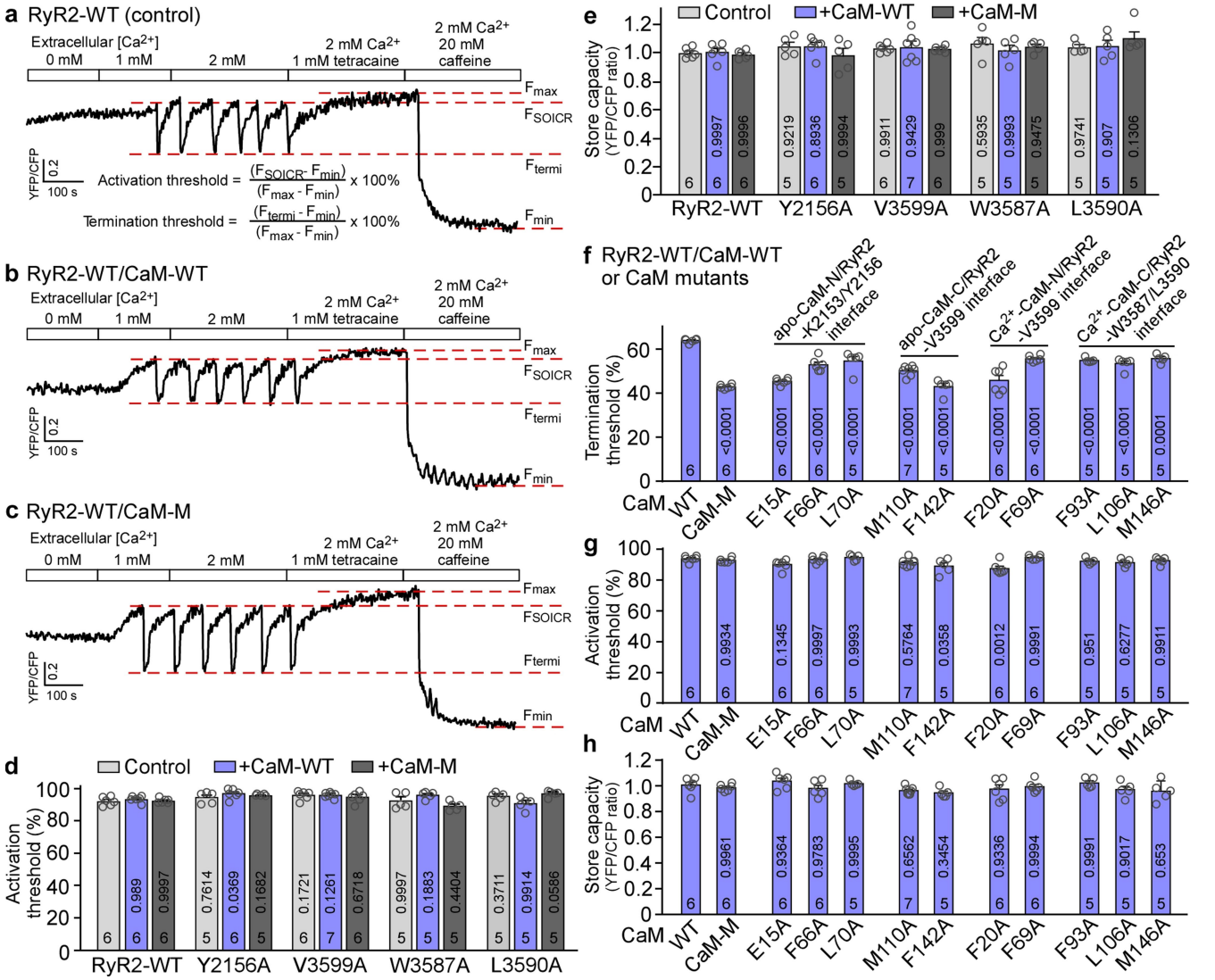

Extended Data Fig. 7 | Effect of RyR2 and CaM mutations on the termination of Ca^{2+} release in HEK293 cells. HEK293 cell lines that express RyR2(WT) and RyR2 mutants were co-transfected with the FRET-based endoplasmic-reticulum luminal Ca^{2+}-sensing protein D1ER and with no CaM (control), CaM(WT) or the Ca^{2+}-binding-deficient CaM mutant, CaM-M. **a**–**c**, Representative single-cell luminal Ca^{2+} recordings of RyR2(WT) cells transfected with no CaM (**a**; $n = 155$ cells), RyR2(WT) cells transfected with CaM(WT) (**b**; $n = 178$ cells) and RyR2-WT cells transfected with CaM-M (**c**; $n = 177$ cells) are shown. F_{SOICR} indicates the FRET level at which SOICR occurs and F_{termi} represents the FRET level at which SOICR terminates. The signal F_{max} is defined as the FRET level after tetracaine treatment. The minimum FRET signal maximum FRET F_{min} is defined as the FRET level after caffeine treatment. **d**, The activation threshold was determined as shown in **a**. **e**, The store capacity was calculated by subtracting F_{min} from F_{max}. **d**, **e**, Data are mean ± s.e.m. with the number of independent experiments for each condition shown on the graph and analysed by one-way ANOVA with a Dunnett's post hoc test (versus RyR2(WT) control) and adjusted P values are indicated. **f**–**h**, RyR2(WT) cells were co-transfected with the FRET-based endoplasmic-reticulum luminal Ca^{2+}-sensing protein D1ER and CaM(WT) or CaM mutants (CaM-M, CaM(E15A), CaM(F66A), CaM(L70A), CaM(M110A), CaM(F142A), CaM(F20A), CaM(F69A), CaM(F93A), CaM(L106A) and CaM(M146A)). CaM mutations close to a specific CaM–RyR2 interface are grouped and are indicated. The termination threshold (**f**), activation threshold (**g**) and store capacity (**h**) were determined as described in **a**–**e** above. **f**–**h**, Data are mean ± s.e.m. with the number of independent experiments for each condition shown on the graph and analysed by one-way ANOVA with a Dunnett's post hoc test (versus CaM(WT)) and adjusted P values are indicated.

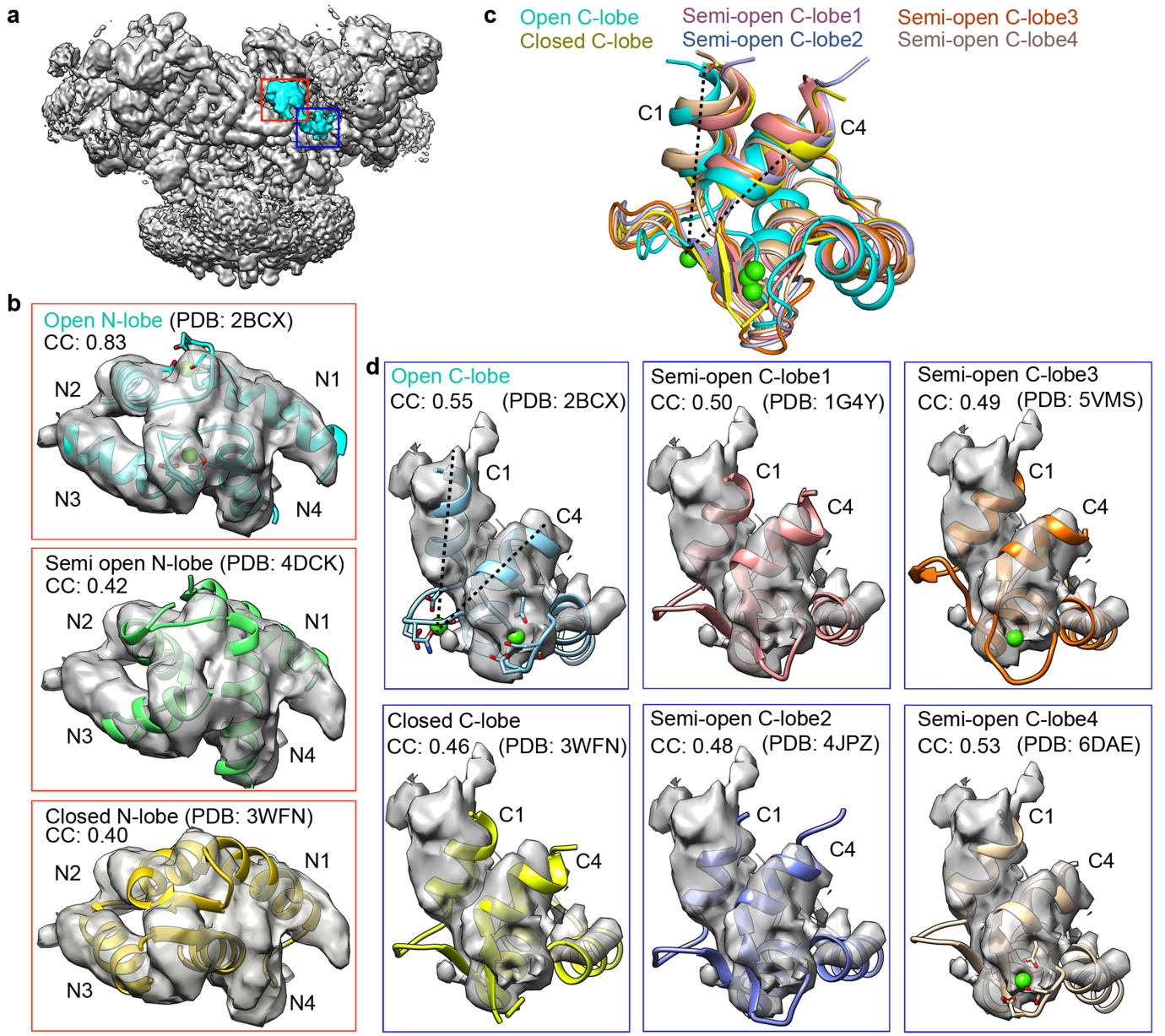

Extended Data Fig. 8 | Evaluation of the conformations of N- and C-lobes of CaM in the FKBP12.6/ATP/caffeine/high-[Ca^{2+}]/Ca^{2+}-CaM structures. a, The electron microscopy map (low-pass-filtered to 4.8 Å resolution at a contour level of 0.015) of FKBP12.6/ATP/caffeine/high-[Ca^{2+}]/Ca^{2+}-CaM. Red and blue boxes indicate the N- and C-lobes, respectively. **b**, Docking of the three reported conformations of the N-lobe of CaM into our electron microscopy map suggests an open conformation of the N-lobe in FKBP12.6/ATP/caffeine/high-[Ca^{2+}]/Ca^{2+}-CaM. CC indicates the cross-correlation coefficient. **c**, An important distinction between C-lobes in the open and semi-open or closed states is the enlarged angle between helices C1 and C4. **d**, Docking analysis supports the open conformation of the C-lobe in FKBP12.6/ATP/caffeine/high-[Ca^{2+}]/Ca^{2+}-CaM.

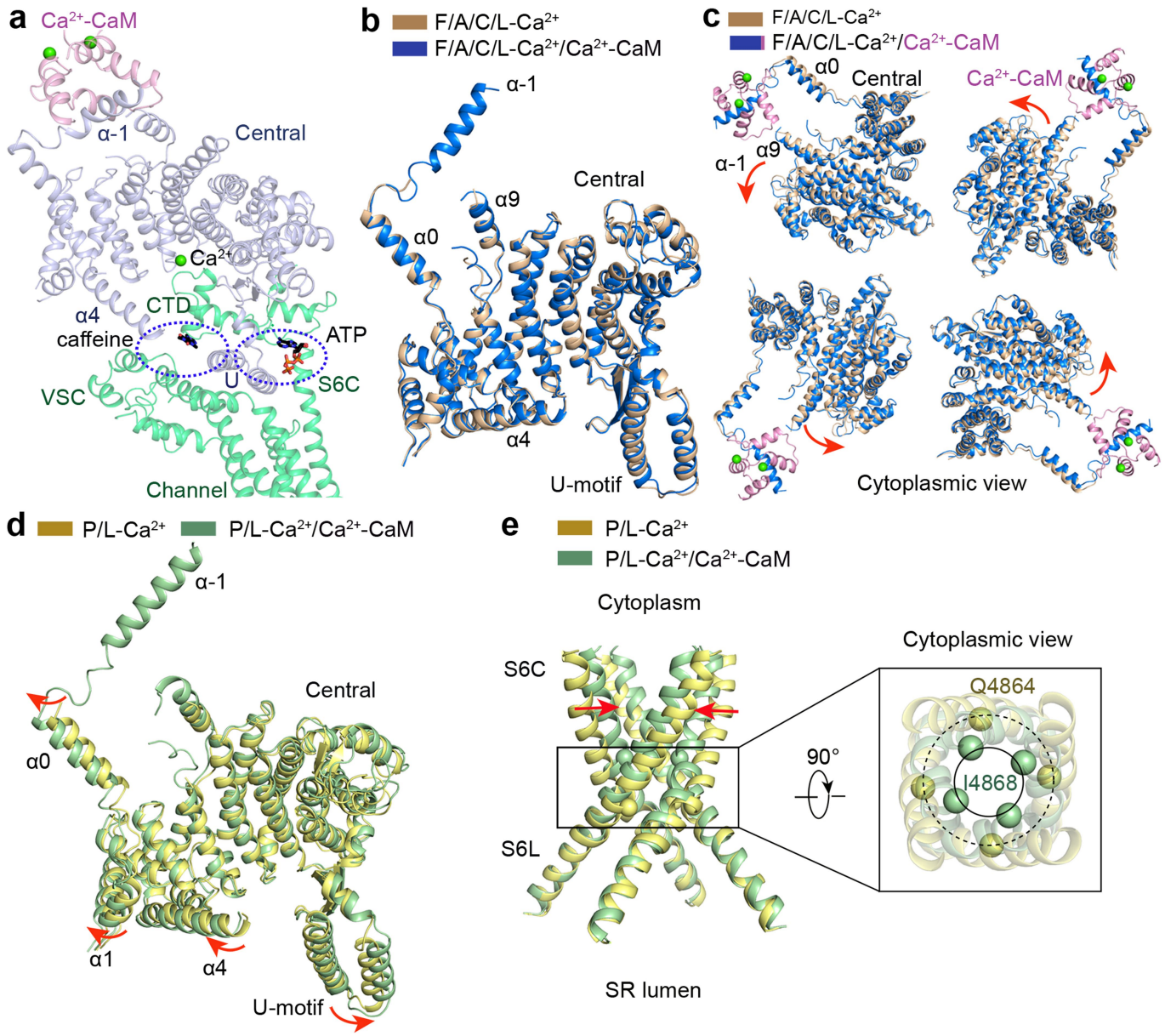

Extended Data Fig. 9 | Inhibitory mechanism of RyR2 by Ca^{2+}-CaM. **a**, Both caffeine and ATP are located at the interfaces between the U-motif and O-ring, locking these elements into a stable unit. **b**, There is almost no intradomain rearrangement of the individual central domain between the structures of FKBP12.6/ATP/caffeine/low-[Ca^{2+}] and FKBP12.6/ATP/caffeine/low-[Ca^{2+}]/Ca^{2+}-CaM. **c**, Ca^{2+}-CaM induces anticlockwise rotation of the overall central domain in FKBP12.6/ATP/caffeine/low-[Ca^{2+}]/Ca^{2+}-CaM when viewed from the cytoplasmic side. The overall tetrameric FKBP12.6/ATP/caffeine/low-[Ca^{2+}]/Ca^{2+}-CaM and FKBP12.6/ATP/caffeine/low-[Ca^{2+}] RyR2 structures are superimposed relative to C-terminal subdomain of the channel domain. Red arrows indicate the conformational changes upon Ca^{2+}-CaM binding. **d**, Ca^{2+}-CaM induces intradomain shifts of the individual central domain in the PCB95 and Ca^{2+}-activated channel. **e**, The PCB95 and Ca^{2+}-activated channel closes after Ca^{2+}-CaM loading.

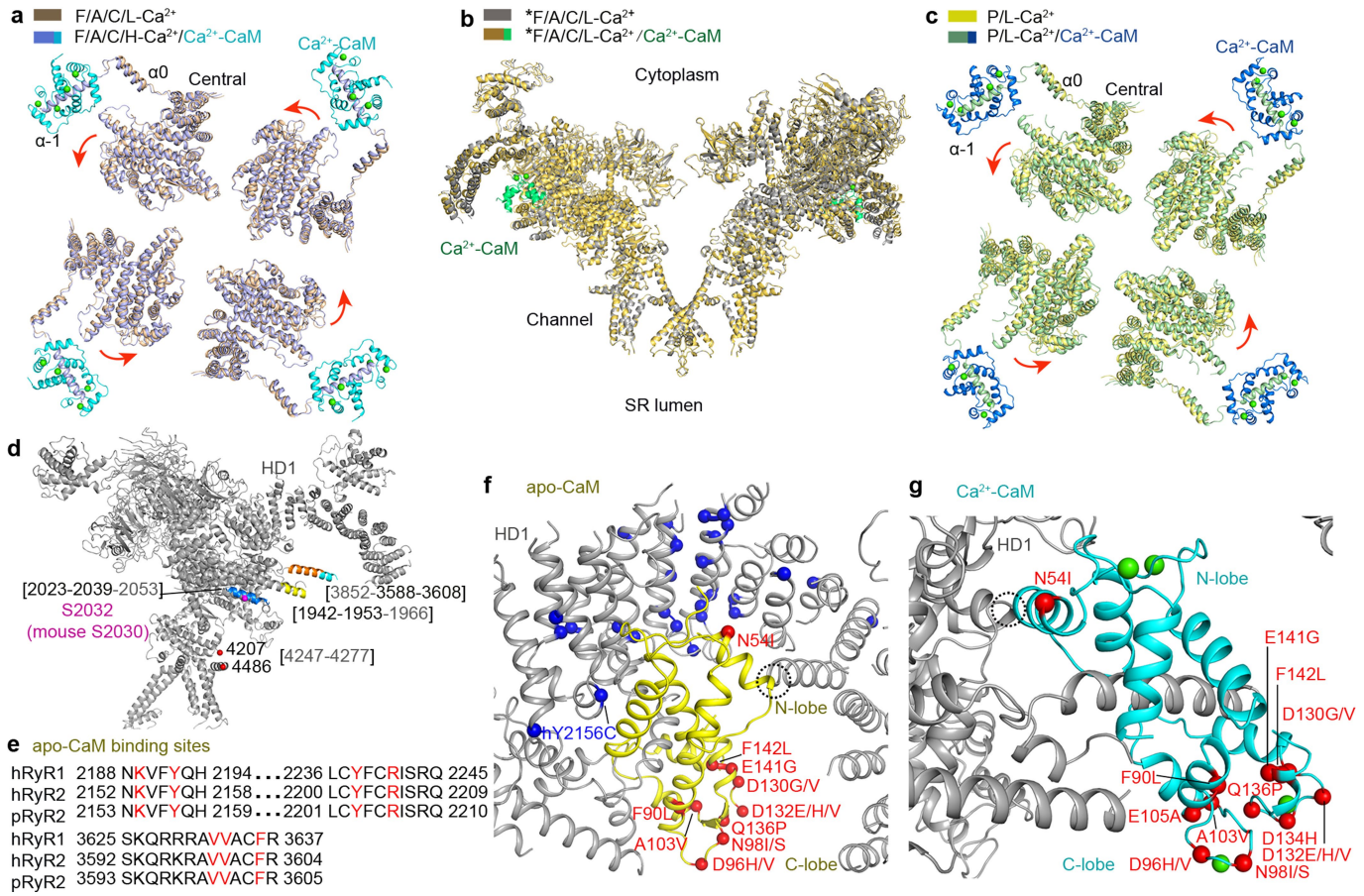

Extended Data Fig. 10 | Conformational changes induced by Ca^{2+}-CaM and mapping of previously identified CaM-binding sequences and disease-associated point mutations onto the structures of RyR2–CaM complexes. a, Compared to FKBP12.6/ATP/caffeine/low-[Ca^{2+}], the four central domains in the FKBP12.6/ATP/caffeine/high-[Ca^{2+}]/Ca^{2+}-CaM RyR2 structure undergo an anticlockwise rotation. The overall tetrameric FKBP12.6/ATP/caffeine/low-[Ca^{2+}] and FKBP12.6/ATP/caffeine/high-[Ca^{2+}]/Ca^{2+}-CaM RyR2 structures are superimposed relative to the C-terminal subdomain of the channel domain. **b**, Compared to the CHAPS- and DOPC-treated FKBP12.6/ATP/caffeine/low-[Ca^{2+}] RyR2 structure, almost no conformational change was induced by Ca^{2+}-CaM in the CHAPS- and DOPC-treated FKBP12.6/ATP/caffeine/low-[Ca^{2+}]/Ca^{2+}-CaM RyR2 structure. **c**, Compared to the PCB95/low-[Ca^{2+}] RyR2 structure, the overall central domain in the PCB95/low-[Ca^{2+}]/Ca^{2+}-CaM RyR2 structure undergoes an anticlockwise rotation. The overall tetrameric PCB95/low-[Ca^{2+}] and PCB95/low-[Ca^{2+}]/Ca^{2+}-CaM RyR2 structures are superimposed relative to the C-terminal subdomain of the channel domain. **d**, Structural mapping of previously reported CaM-binding sequences. Orange, the overlapping binding sequences of apo-CaM and Ca^{2+}-CaM; cyan, the binding sequence of Ca^{2+}-CaM; yellow, the binding sequence of apo-CaM; blue, segments that are not involved in binding in our structures; red, sequences that are invisible in the structures. The residue numbers in brackets that are labelled grey indicate that the sequences are invisible in the structure. **e**, The primary apo-CaM binding sequences in RyR2 are the same in RyR1. Red residues highlight the key contact residues. **f**, Mapping of the disease-associated point mutations onto the structure of the RyR2–apo-CaM complex. The mutations in HD1 and apo-CaM are coloured blue and red, respectively. **g**, Mapping of the CaM disease-associated point mutations onto the structure of the RyR2–Ca^{2+}-CaM complex.

Extended Data Table 1 | Cryo-EM data collection, refinement and validation statistics

	F/apo-CaM (EMDB-9833) (PDB 6JI8)	F/A/C/L-Ca^{2+}/CaM-M (EMDB-9834) (PDB 6JII)	F/A/C/L-Ca^{2+} (EMDB-9831) (PDB 6JI0)	F/A/C/L-Ca^{2+}/Ca^{2+}-CaM (EMDB-9836) (PDB 6JIU)	*F/A/C/L-Ca^{2+} (EMDB-9879) (PDB 6JRR)	*F/A/C/L-Ca^{2+}/Ca^{2+}-CaM (EMDB-9880) (PDB 6JRS)	F/A/C/H-Ca^{2+}/Ca^{2+}-CaM (EMDB-9837) (PDB 6JIY)	P/L-Ca^{2+}/Ca^{2+}-CaM (EMDB-9889) (PDB 6JV2)
Data collection and processing								
Magnification	105,000	105,000	105,000	105,000	105,000	105,000	105,000	105,000
Voltage (kV)	300	300	300	300	300	300	300	300
Electron exposure (e–/Å^2)	45.6	50	50	45.6	50	50	50	50
Defocus range (μm)	-0.8~-1.8	-1.3~-1.7	-1.3~-1.7	-0.8~-1.8	-1.3~-1.7	-1.3~-1.7	-1.3~-1.7	-1.3~-1.7
Pixel size (Å)	1.338	1.091	1.091	1.338	1.091	1.091	1.091	1.091
Symmetry imposed	C4	C4	C4	C4	C4	C4	C4	C4
Initial particle images (no.)	1,180,104	404,978	515,941	1,026,058	769,264	666,134	595,005	759,504
Final particle images (no.)	208,715	69,556	78,841	77,029	149,212	154,111	96,158	22,876
Map resolution (Å)	3.6	4.2	4.2	4.2	3.9	3.7	3.9	4.4
FSC threshold	0.143	0.143	0.143	0.143	0.143	0.143	0.143	0.143
Map resolution range (Å)	535.2-3.6	436.4-4.2	436.4-4.2	535.2-4.2	436.4-3.9	436.4-3.7	436.4-3.9	436.4-4.4
Refinement								
Initial model used (PDB code)	5GOA	5GOA	5GOA	5GOA	5GOA	5GOA	5GOA	5GOA
Model resolution (Å)	3.6	4.2	4.2	4.2	3.9	3.7	3.9	4.4
FSC threshold	0.143	0.143	0.143	0.143	0.143	0.143	0.143	0.143
Model resolution range (Å)	535.2-3.6	436.4-4.2	436.4-4.2	535.2-4.2	436.4-3.9	436.4-3.7	436.4-3.9	436.4-4.4
Map sharpening *B* factor (Å^2)	-169	-167	-181	-167	-174	-161	-181	-64
Model composition								
Non-hydrogen atoms	115,060	115,028	109,772	112,212	109,132	112,208	115,288	111,080
Protein residues	15,024	15,012	14,332	14,684	14,268	14,660	15,056	14,564
Ligands	4	16	16	24	16	24	32	24
B factors (Å^2)								
Protein	79.52	192.63	147.15	226.13	118.38	103.61	122.58	303.05
Ligand	76.76	97.59	75.47	158.62	50.84	41.76	71.04	574.56
R.m.s. deviations								
Bond lengths (Å)	0.010	0.008	0.007	0.006	0.010	0.009	0.007	0.011
Bond angles (°)	1.250	1.096	1.123	0.981	1.111	1.050	1.033	1.292
Validation								
MolProbity score	2.06	2.01	2.03	2.11	2.02	2.08	2.04	2.63
Clashscore	8.56	7.61	7.43	10.69	8.45	8.70	7.78	19.3
Poor rotamers (%)	1.06	0.59	0.88	0.53	0.81	0.91	0.47	1.93
Ramachandran plot								
Favored (%)	89.0	88.4	86.9	89.5	89.5	87.3	87.5	86.5
Allowed (%)	10.5	11.2	12.9	10.3	10.2	12.4	12.2	13.3
Disallowed (%)	0.5	0.4	0.2	0.2	0.3	0.3	0.3	0.2

nature research

Corresponding author(s): Deshun Gong; S.R. Wayne Chen; Nieng Yan

Last updated by author(s): May 23, 2019

Reporting Summary

Nature Research wishes to improve the reproducibility of the work that we publish. This form provides structure for consistency and transparency in reporting. For further information on Nature Research policies, see Authors & Referees and the Editorial Policy Checklist.

Statistics

For all statistical analyses, confirm that the following items are present in the figure legend, table legend, main text, or Methods section.

n/a	Confirmed	
☐	☒	The exact sample size (*n*) for each experimental group/condition, given as a discrete number and unit of measurement
☐	☒	A statement on whether measurements were taken from distinct samples or whether the same sample was measured repeatedly
☐	☒	The statistical test(s) used AND whether they are one- or two-sided *Only common tests should be described solely by name; describe more complex techniques in the Methods section.*
☒	☐	A description of all covariates tested
☐	☒	A description of any assumptions or corrections, such as tests of normality and adjustment for multiple comparisons
☐	☒	A full description of the statistical parameters including central tendency (e.g. means) or other basic estimates (e.g. regression coefficient) AND variation (e.g. standard deviation) or associated estimates of uncertainty (e.g. confidence intervals)
☒	☐	For null hypothesis testing, the test statistic (e.g. *F*, *t*, *r*) with confidence intervals, effect sizes, degrees of freedom and *P* value noted *Give P values as exact values whenever suitable.*
☒	☐	For Bayesian analysis, information on the choice of priors and Markov chain Monte Carlo settings
☐	☐	For hierarchical and complex designs, identification of the appropriate level for tests and full reporting of outcomes
☒	☐	Estimates of effect sizes (e.g. Cohen's *d*, Pearson's *r*), indicating how they were calculated

Our web collection on statistics for biologists contains articles on many of the points above.

Software and code

Policy information about availability of computer code

Data collection	AutoEMationII; Compix Simple PCI 6; Axopatch 200A amplifier
Data analysis	Relion 2.0; Thunder; MotionCor2 1.1.0; GCTF 1.06; Phenix 1.12; Coot 0.8.6; Pymol 1.8.6.0; Chimera 1.11; pclamp 8.1; Compix Simple PCI 6, GraphPad Prism 8.1.

For manuscripts utilizing custom algorithms or software that are central to the research but not yet described in published literature, software must be made available to editors/reviewers. We strongly encourage code deposition in a community repository (e.g. GitHub). See the Nature Research guidelines for submitting code & software for further information.

Data

Policy information about availability of data

All manuscripts must include a data availability statement. This statement should provide the following information, where applicable:

- Accession codes, unique identifiers, or web links for publicly available datasets
- A list of figures that have associated raw data
- A description of any restrictions on data availability

Atomic coordinates and EM density maps of the F/apo-CaM (PDB: 6JI8; EMDB: EMD-9833), F/A/C/L-Ca2+/CaM-M (PDB: 6JII; EMDB: EMD-9834), F/A/C/L-Ca2+ (PDB: 6JI0; EMDB: EMD-9831), F/A/C/L-Ca2+/Ca2+-CaM (PDB: 6JIU; EMDB: EMD-9836), *F/A/C/L-Ca2+ (PDB: 6JRR; EMDB: EMD-9879), *F/A/C/L-Ca2+/Ca2+-CaM (PDB: 6JRS; EMDB: EMD-9880), F/A/C/H-Ca2+/Ca2+-CaM (PDB: 6JIY; EMDB: EMD-9837), and P/L-Ca2+/Ca2+-CaM (PDB: 6JV2; EMDB: EMD-9889) structures have been deposited in the Protein Data Bank (http://www.rcsb.org) and the Electron Microscopy Data Bank (https://www.ebi.ac.uk/pdbe/emdb/). Source Data for Fig. 2e, f and Extended Data Figs. 1c, 6f, 7d-h are available online. All other data are available from the corresponding authors upon reasonable request.

Field-specific reporting

Please select the one below that is the best fit for your research. If you are not sure, read the appropriate sections before making your selection.

☒ Life sciences ☐ Behavioural & social sciences ☐ Ecological, evolutionary & environmental sciences

For a reference copy of the document with all sections, see nature.com/documents/nr-reporting-summary-flat.pdf

Life sciences study design

All studies must disclose on these points even when the disclosure is negative.

Sample size	No sample size calculation was predetermined. We chose the sample size based on our previous studies that would be sufficient for testing for differences between groups.
Data exclusions	No data were excluded.
Replication	All experiments were repeated at least 5 times with similar results.
Randomization	No animals were involved in this study. Samples (cells or single channels) were not randomized for experiments in this study.
Blinding	Single channel recording and single cell calcium imaging experiments were not blinded, but the same recording and imaging conditions (solutions and recording/imaging settings) were applied to all channels and cell groups.

Behavioural & social sciences study design

All studies must disclose on these points even when the disclosure is negative.

Study description	*Briefly describe the study type including whether data are quantitative, qualitative, or mixed-methods (e.g. qualitative cross-sectional, quantitative experimental, mixed-methods case study).*
Research sample	*State the research sample (e.g. Harvard university undergraduates, villagers in rural India) and provide relevant demographic information (e.g. age, sex) and indicate whether the sample is representative. Provide a rationale for the study sample chosen. For studies involving existing datasets, please describe the dataset and source.*
Sampling strategy	*Describe the sampling procedure (e.g. random, snowball, stratified, convenience). Describe the statistical methods that were used to predetermine sample size OR if no sample-size calculation was performed, describe how sample sizes were chosen and provide a rationale for why these sample sizes are sufficient. For qualitative data, please indicate whether data saturation was considered, and what criteria were used to decide that no further sampling was needed.*
Data collection	*Provide details about the data collection procedure, including the instruments or devices used to record the data (e.g. pen and paper, computer, eye tracker, video or audio equipment) whether anyone was present besides the participant(s) and the researcher, and whether the researcher was blind to experimental condition and/or the study hypothesis during data collection.*
Timing	*Indicate the start and stop dates of data collection. If there is a gap between collection periods, state the dates for each sample cohort.*
Data exclusions	*If no data were excluded from the analyses, state so OR if data were excluded, provide the exact number of exclusions and the rationale behind them, indicating whether exclusion criteria were pre-established.*
Non-participation	*State how many participants dropped out/declined participation and the reason(s) given OR provide response rate OR state that no participants dropped out/declined participation.*
Randomization	*If participants were not allocated into experimental groups, state so OR describe how participants were allocated to groups, and if allocation was not random, describe how covariates were controlled.*

Ecological, evolutionary & environmental sciences study design

All studies must disclose on these points even when the disclosure is negative.

Study description	*Briefly describe the study. For quantitative data include treatment factors and interactions, design structure (e.g. factorial, nested, hierarchical), nature and number of experimental units and replicates.*
Research sample	*Describe the research sample (e.g. a group of tagged Passer domesticus, all Stenocereus thurberi within Organ Pipe Cactus National Monument), and provide a rationale for the sample choice. When relevant, describe the organism taxa, source, sex, age range and any manipulations. State what population the sample is meant to represent when applicable. For studies involving existing datasets,*

	describe the data and its source.
Sampling strategy	*Note the sampling procedure. Describe the statistical methods that were used to predetermine sample size OR if no sample-size calculation was performed, describe how sample sizes were chosen and provide a rationale for why these sample sizes are sufficient.*
Data collection	*Describe the data collection procedure, including who recorded the data and how.*
Timing and spatial scale	*Indicate the start and stop dates of data collection, noting the frequency and periodicity of sampling and providing a rationale for these choices. If there is a gap between collection periods, state the dates for each sample cohort. Specify the spatial scale from which the data are taken*
Data exclusions	*If no data were excluded from the analyses, state so OR if data were excluded, describe the exclusions and the rationale behind them, indicating whether exclusion criteria were pre-established.*
Reproducibility	*Describe the measures taken to verify the reproducibility of experimental findings. For each experiment, note whether any attempts to repeat the experiment failed OR state that all attempts to repeat the experiment were successful.*
Randomization	*Describe how samples/organisms/participants were allocated into groups. If allocation was not random, describe how covariates were controlled. If this is not relevant to your study, explain why.*
Blinding	*Describe the extent of blinding used during data acquisition and analysis. If blinding was not possible, describe why OR explain why blinding was not relevant to your study.*

Did the study involve field work? ☐ Yes ☐ No

Field work, collection and transport

Field conditions	*Describe the study conditions for field work, providing relevant parameters (e.g. temperature, rainfall).*
Location	*State the location of the sampling or experiment, providing relevant parameters (e.g. latitude and longitude, elevation, water depth).*
Access and import/export	*Describe the efforts you have made to access habitats and to collect and import/export your samples in a responsible manner and in compliance with local, national and international laws, noting any permits that were obtained (give the name of the issuing authority, the date of issue, and any identifying information).*
Disturbance	*Describe any disturbance caused by the study and how it was minimized.*

Reporting for specific materials, systems and methods

We require information from authors about some types of materials, experimental systems and methods used in many studies. Here, indicate whether each material, system or method listed is relevant to your study. If you are not sure if a list item applies to your research, read the appropriate section before selecting a response.

Materials & experimental systems

n/a	Involved in the study
☒	☐ Antibodies
☐	☒ Eukaryotic cell lines
☒	☐ Palaeontology
☐	☒ Animals and other organisms
☒	☐ Human research participants
☒	☐ Clinical data

Methods

n/a	Involved in the study
☒	☐ ChIP-seq
☒	☐ Flow cytometry
☒	☐ MRI-based neuroimaging

Antibodies

Antibodies used	*Describe all antibodies used in the study; as applicable, provide supplier name, catalog number, clone name, and lot number.*
Validation	*Describe the validation of each primary antibody for the species and application, noting any validation statements on the manufacturer's website, relevant citations, antibody profiles in online databases, or data provided in the manuscript.*

Eukaryotic cell lines

Policy information about cell lines

Cell line source(s)	The Flp-In T-REx HEK293 Cell Line was obtained from Invitrogen

Authentication	Not authenticated
Mycoplasma contamination	These cells tested negative for mycoplasma contamination
Commonly misidentified lines (See ICLAC register)	No commonly misidentified cell lines were used in this study.

Palaeontology

Specimen provenance	*Provide provenance information for specimens and describe permits that were obtained for the work (including the name of the issuing authority, the date of issue, and any identifying information).*
Specimen deposition	*Indicate where the specimens have been deposited to permit free access by other researchers.*
Dating methods	*If new dates are provided, describe how they were obtained (e.g. collection, storage, sample pretreatment and measurement), where they were obtained (i.e. lab name), the calibration program and the protocol for quality assurance OR state that no new dates are provided.*

☐ Tick this box to confirm that the raw and calibrated dates are available in the paper or in Supplementary Information.

Animals and other organisms

Policy information about studies involving animals; ARRIVE guidelines recommended for reporting animal research

Laboratory animals	The porcine hearts were bought from meat processing factory
Wild animals	NA
Field-collected samples	NA
Ethics oversight	NA

Note that full information on the approval of the study protocol must also be provided in the manuscript.

Human research participants

Policy information about studies involving human research participants

Population characteristics	*Describe the covariate-relevant population characteristics of the human research participants (e.g. age, gender, genotypic information, past and current diagnosis and treatment categories). If you filled out the behavioural & social sciences study design questions and have nothing to add here, write "See above."*
Recruitment	*Describe how participants were recruited. Outline any potential self-selection bias or other biases that may be present and how these are likely to impact results.*
Ethics oversight	*Identify the organization(s) that approved the study protocol.*

Note that full information on the approval of the study protocol must also be provided in the manuscript.

Clinical data

Policy information about clinical studies

All manuscripts should comply with the ICMJE guidelines for publication of clinical research and a completed CONSORT checklist must be included with all submissions.

Clinical trial registration	*Provide the trial registration number from ClinicalTrials.gov or an equivalent agency.*
Study protocol	*Note where the full trial protocol can be accessed OR if not available, explain why.*
Data collection	*Describe the settings and locales of data collection, noting the time periods of recruitment and data collection.*
Outcomes	*Describe how you pre-defined primary and secondary outcome measures and how you assessed these measures.*

ChIP-seq

Data deposition

☐ Confirm that both raw and final processed data have been deposited in a public database such as GEO.

☐ Confirm that you have deposited or provided access to graph files (e.g. BED files) for the called peaks.

Data access links
May remain private before publication.

For "Initial submission" or "Revised version" documents, provide reviewer access links. For your "Final submission" document, provide a link to the deposited data.

Files in database submission

Provide a list of all files available in the database submission.

Genome browser session
(e.g. UCSC)

Provide a link to an anonymized genome browser session for "Initial submission" and "Revised version" documents only, to enable peer review. Write "no longer applicable" for "Final submission" documents.

Methodology

Replicates

Describe the experimental replicates, specifying number, type and replicate agreement.

Sequencing depth

Describe the sequencing depth for each experiment, providing the total number of reads, uniquely mapped reads, length of reads and whether they were paired- or single-end.

Antibodies

Describe the antibodies used for the ChIP-seq experiments; as applicable, provide supplier name, catalog number, clone name, and lot number.

Peak calling parameters

Specify the command line program and parameters used for read mapping and peak calling, including the ChIP, control and index files used.

Data quality

Describe the methods used to ensure data quality in full detail, including how many peaks are at FDR 5% and above 5-fold enrichment.

Software

Describe the software used to collect and analyze the ChIP-seq data. For custom code that has been deposited into a community repository, provide accession details.

Flow Cytometry

Plots

Confirm that:

☐ The axis labels state the marker and fluorochrome used (e.g. CD4-FITC).

☐ The axis scales are clearly visible. Include numbers along axes only for bottom left plot of group (a 'group' is an analysis of identical markers).

☐ All plots are contour plots with outliers or pseudocolor plots.

☐ A numerical value for number of cells or percentage (with statistics) is provided.

Methodology

Sample preparation

Describe the sample preparation, detailing the biological source of the cells and any tissue processing steps used.

Instrument

Identify the instrument used for data collection, specifying make and model number.

Software

Describe the software used to collect and analyze the flow cytometry data. For custom code that has been deposited into a community repository, provide accession details.

Cell population abundance

Describe the abundance of the relevant cell populations within post-sort fractions, providing details on the purity of the samples and how it was determined.

Gating strategy

Describe the gating strategy used for all relevant experiments, specifying the preliminary FSC/SSC gates of the starting cell population, indicating where boundaries between "positive" and "negative" staining cell populations are defined.

☐ Tick this box to confirm that a figure exemplifying the gating strategy is provided in the Supplementary Information.

Magnetic resonance imaging

Experimental design

Design type

Indicate task or resting state; event-related or block design.

Design specifications

Specify the number of blocks, trials or experimental units per session and/or subject, and specify the length of each trial or block (if trials are blocked) and interval between trials.

Behavioral performance measures

State number and/or type of variables recorded (e.g. correct button press, response time) and what statistics were used to establish that the subjects were performing the task as expected (e.g. mean, range, and/or standard deviation across subjects).

Acquisition

Imaging type(s) — *Specify: functional, structural, diffusion, perfusion.*

Field strength — *Specify in Tesla*

Sequence & imaging parameters — *Specify the pulse sequence type (gradient echo, spin echo, etc.), imaging type (EPI, spiral, etc.), field of view, matrix size, slice thickness, orientation and TE/TR/flip angle.*

Area of acquisition — *State whether a whole brain scan was used OR define the area of acquisition, describing how the region was determined.*

Diffusion MRI ☐ Used ☐ Not used

Preprocessing

Preprocessing software — *Provide detail on software version and revision number and on specific parameters (model/functions, brain extraction, segmentation, smoothing kernel size, etc.).*

Normalization — *If data were normalized/standardized, describe the approach(es): specify linear or non-linear and define image types used for transformation OR indicate that data were not normalized and explain rationale for lack of normalization.*

Normalization template — *Describe the template used for normalization/transformation, specifying subject space or group standardized space (e.g. original Talairach, MNI305, ICBM152) OR indicate that the data were not normalized.*

Noise and artifact removal — *Describe your procedure(s) for artifact and structured noise removal, specifying motion parameters, tissue signals and physiological signals (heart rate, respiration).*

Volume censoring — *Define your software and/or method and criteria for volume censoring, and state the extent of such censoring.*

Statistical modeling & inference

Model type and settings — *Specify type (mass univariate, multivariate, RSA, predictive, etc.) and describe essential details of the model at the first and second levels (e.g. fixed, random or mixed effects; drift or auto-correlation).*

Effect(s) tested — *Define precise effect in terms of the task or stimulus conditions instead of psychological concepts and indicate whether ANOVA or factorial designs were used.*

Specify type of analysis: ☐ Whole brain ☐ ROI-based ☐ Both

Statistic type for inference (See Eklund et al. 2016) — *Specify voxel-wise or cluster-wise and report all relevant parameters for cluster-wise methods.*

Correction — *Describe the type of correction and how it is obtained for multiple comparisons (e.g. FWE, FDR, permutation or Monte Carlo).*

Models & analysis

n/a	Involved in the study
☐	☐ Functional and/or effective connectivity
☐	☐ Graph analysis
☐	☐ Multivariate modeling or predictive analysis

Functional and/or effective connectivity — *Report the measures of dependence used and the model details (e.g. Pearson correlation, partial correlation, mutual information).*

Graph analysis — *Report the dependent variable and connectivity measure, specifying weighted graph or binarized graph, subject- or group-level, and the global and/or node summaries used (e.g. clustering coefficient, efficiency, etc.).*

Multivariate modeling and predictive analysis — *Specify independent variables, features extraction and dimension reduction, model, training and evaluation metrics.*